Event-Based Sensing and Multimodal AI Architectures for Underwater Acoustic Sensing

Sofia Marques Duarte
Master in Engineering Physics
Department of Physics and Astronomy
Faculty of Sciences of the University of Porto
Faculty of Engineering of the University of Porto
2026

Event-Based Sensing and Multimodal AI Architectures for Underwater Acoustic Sensing

Sofia Marques Duarte

Project Report carried out as part of the Master in Engineering Physics

Department of Physics and Astronomy

2026



Supervisor
Dr. Nuno Azevedo Silva, Area Manager, INESC TEC

Co-supervisor
Dra. Catarina Silva Monteiro, Assistant Researcher, INESC TEC

Acknowledgements

Não posso deixar de expressar o meu agradecimento a todas as pessoas que me acompanharam e contribuíram para a realização desta tese.

Primeiramente, agradeço aos meus orientadores Dr. Nuno Silva e Dra. Catarina Monteiro por toda a ajuda prestada, especialmente nos momentos em que achava que já não dava para ir mais longe. Por terem tornado também esta etapa normalmente custosa e desafiadora, mais leve e divertida.

Agradeço igualmente a todos os restantes professores, investigadores e estudantes do Centro de Fotónica Aplicada do INESC TEC pela excelente integração, por todos os convívios e pela ajuda ao longo destes meses.

Por último, deixo um agradecimento muito especial aos meus queridos pais e ao meu irmão por todo o apoio incondicional e encorajamento desde sempre. Também aos meus amigos e namorado pelos momentos e presença constante.

Resumo

A expansão das aplicações subaquáticas, nomeadamente a monitorização de infraestruturas offshore e a segurança marítima - onde a baixa visibilidade e a dispersão da luz limitam o uso dos sensores óticos - está a revolucionar o mundo dos sensores acústicos. As soluções atuais dependem de hidrofones piezoelétricos, que podem ser dispendiosos e difíceis de escalar. Como tal, os sensores de fibra ótica constituem uma alternativa promissora devido à sua imunidade eletromagnética e robustez em ambientes mais adversos. No entanto muitas abordagens requerem sistemas de interrogação complexos e, por isso, os sensores de fibra ótica baseados no padrão de speckle surgem como uma abordagem alternativa. O ponto a reter para o desenvolvimento deste trabalho é que as perturbações acústicas externas alteram a interferência modal, modificando o padrão de speckle à saída da fibra ótica multimodo. Para capturar estas variações do speckle de forma eficiente são usadas as câmaras de eventos (EVS) que detetam de forma assíncrona alterações de intensidade ao nível do pixel, permitindo uma elevada resolução temporal, um baixo volume de dados e também uma possível monitorização simultânea de múltiplas fibras, ao contrário das câmaras tradicionais com sensores CMOS e CCD, que são limitadas em termos de resolução temporal. Neste trabalho demonstraremos um sistema de deteção baseado no padrão de speckle para deteção e localização das fontes acústicas, abrindo possibilidades para inúmeras aplicações subaquáticas e também para integração em veículos robóticos. Para isso, o padrão de speckle à saída foi projetado numa câmara de eventos, e utilizaram-se polarizadores lineares para ajustar a potência ótica e melhorar a resposta do speckle detetada. O sistema foi inicialmente caracterizado no ar, para frequências acústicas entre 1 Hz e 1 kHz, onde foi detetada uma excitação acústica a distâncias entre a fonte e a fibra de até 1 m, com uma relação sinal-ruído máxima de 25 dB. Em seguida, avaliámos o mesmo princípio de deteção num tanque de água com 5 metros de profundidade, utilizando um modem acústico omnidirecional horizontal EvoLogics que emitia sinais entre 18 e 34 kHz. Com a fibra submersa, foram detetados sinais acústicos a distâncias de até 3 m. De seguida, como prova de conceito, o sistema foi avaliado em relação às suas capacidades de localização num plano, onde os atrasos temporais obtidos a partir da câmara de eventos são mapeados para posições de impactos acústicos através de um modelo de regressão KNN, ou também a partir de um modelo físico. Os resultados preliminares demonstram o potencial da abordagem proposta para localização de perturbações à superfície, com um erro máximo de 49 cm, embora se esperem melhorias futuras para eliminar estes outliers e aumentar a robustez.

No que diz respeito à deteção baseada na polarização, foram detetadas frequências até sensivelmente os 8 kHz com uma relação sinal-ruído satisfatória debaixo de água com um polarímetro comercial, tanto com a fibra em espiral como esticada, com esta última configuração a apresentar uma maior relação sinal-ruído. O complemento do estudo da polarização é vantajosa pois fornece informação adicional, ao mesmo tempo que proporciona uma largura de banda maior do que a obtida apenas com sistemas de deteção baseados no padrão de speckle.

Noutro segmento, foi estudada a classificação a partir das variações do estado de polarização da luz à saída da fibra, enquanto se explorou a possibilidade de uma sinergia entre os dados extraídos da câmara de eventos e do polarímetro, de modo a permitir localizar e classificar as fontes acústicas, simultaneamente. Os resultados finais mostraram um erro médio de 17,8 cm na localização de fontes acústicas e uma precisão média de $96.34 \pm 1.66\%$ na classificação usando o modelo KNN.

Palavras-chave: Sensor em fibra ótica, Padrão de Speckle, Polarização, Perceção Ambiental e Consciência Situacional

Abstract

The expansion of underwater applications, namely offshore infrastructure monitoring and maritime security, where low visibility and scattering limit optical imaging, is revolutionizing the world of acoustic sensors. Current solutions rely on piezoelectric hydrophones, which can be costly and difficult to scale. In this way, optical fiber sensors are a promising alternative due to their electromagnetic immunity and robustness in harsh environments. However, many approaches require complex interrogation systems, and that is why speckle-based sensing in multimode fibers appear as an alternative approach. The key point for the development of this thesis is that external acoustic perturbations modify modal interference, changing the output speckle pattern. To capture these speckle variations efficiently, Event Vision Sensors (EVS) asynchronously detect pixel-level intensity changes, enabling high temporal resolution, low data volume, and monitoring of multiple fibers, unlike CMOS/CCD cameras, which are limited in temporal resolution. In this work, we demonstrate a speckle-based sensing system for acoustic detection, source localization, and classification, opening doors for numerous underwater applications and also for robotics integration. For that, the output speckle pattern was projected onto an EVS, and linear polarization control was used to adjust the optical power and improve the detected speckle response. The system was first characterized in air, for acoustic frequencies between 1 Hz to 1 kHz, and detected acoustic excitation at source-to-fiber distances up to 1 m with a maximum signal-to-noise ratio of 25 dB. We then evaluated the same sensing principle underwater in a 5 m deep water tank using an EvoLogics horizontally omnidirectional acoustic modem emitting signals between 18 and 34 kHz. With the fiber submerged, acoustic signals were detected at distances up to 3 m. Thereafter, as proof of concept, the system was evaluated for surface-based localization, where time-delay features obtained from the event cameras are mapped to acoustic impact positions through a K-nearest-neighbor regression model or a physics-based model. The preliminary results demonstrate the potential of the proposed approach for surface-based impact localization, with a maximum error obtained of 49 cm, although further refinement is expected to eliminate these outliers and increase robustness.

Regarding polarization-based sensing, frequencies up to approximately 8 kHz with an acceptable SNR were detected underwater with a commercial polarimeter, both with the fiber coiled and stretched, with the latter exhibiting a higher SNR. Thus, polarization provides additional information while providing larger bandwidth than using speckle-based

sensing systems only.

In another segment, classification was studied based on variations in the polarization state of the light at the fiber output, while exploring the possibility of synergy between data extracted from the event camera and the polarimeter, in order to simultaneously locate and classify acoustic sources. The results showed a mean error of 17.8 cm for acoustic source localization and a mean accuracy of $96.34 \pm 1.66\%$ for classification using a KNN classifier.

Keywords: Optical Fiber based Sensors, Speckle, Polarization, Environmental Perception, Situational Awareness

Table of Contents

List of Figures vii

List of Abbreviations ix

1. Introduction 1
   1.1. Proprioceptive and Exteroceptive sensors for robotics 2
      1.1.1. Acoustic Sensing and optical fiber alternatives 3
   1.2. Objectives and thesis structure 8
   1.3. Thesis outputs 9
2. Event-based Vision for Speckle Interrogation 10
   2.1. From image to event-based vision 11
   2.2. EVS: Data acquisition and processing 15
   2.3. Signal Detection in air 19
   2.4. Signal Detection underwater 22
      2.4.1. Limitations of Interrogation with EVS 23
   2.5. Sound Localization in two dimensions 26
      2.5.1. Localization using KNN Regression Model 27
      2.5.2. Localization using a Physics-based localization Model 29
      2.5.3. Signal Automatic detection 31
   2.6. Concluding Remarks 32
3. State of Polarization Interrogation for Acoustic Signal Classification and Reconstruction 34
   3.1. Experimental Characterization of Polarization-Based Acoustic Sensing 38
   3.2. Sound Source Classification 40
   3.3. Towards low SWaP-C polarimeter setups 41
   3.4. Concluding Remarks 43
4. Multimodal System with Event-Based Vision and Polarization Sensing 45
   4.1. Experimental results: simultaneous localization and classification 46
   4.2. Concluding Remarks 48
5. Final Remarks and Future Work 50

Bibliography 52

List of Figures

1.1. Examples of sensors implemented underwater. (Adapted from Ref. 5, 6) 1
1.2. DAS interrogation scheme (Adapted from Ref. 14). 4
1.3. Physical mechanisms underlying speckle pattern formation: (A) generated on light scattering from rough optical surfaces; (B) generated by modal interference in optical fibers. 5
1.4. Speckle interrogation scheme: propagation of M modes in the fiber. 7

2.1. CCD and CMOS operating principles [48]. 12
2.2. (A) CCD sensor; (B) CMOS sensor; (C) Event-based camera (Adapted from Ref. 50, 51). 13
2.3. Similarities of working principles between human eye and EVS [52]. 14
2.4. Relation between incident light luminance and output voltage on the pixel unit. 15
2.5. (Right) Spatial images obtained from the acquired event stream data (left). 16
2.6. Metavision software overview: Anti-Flicker, ROI, Display and Bias settings. 16
2.7. (Left) Detection of three ROIs automatically after the accumulation of the detected events. (Right) ROIs obtained for each output fiber. 18
2.8. Overall steps for data acquisition and processing. 19
2.9. Setup of the event-based camera with 2 optical fibers. 20
2.10. Illustration of 2 fibers for acoustic signal detection in air: (F) Optical Fibers. 21
2.11. Spectrograms of the signal in air (left); SNR vs applied frequency (right). 21
2.12. (a) Setup with plastic containers; (b) Setup with a PVC pipe; (c) Fiber wrapped around a cork (15-m long); (d) Fiber wrapped around a coil (15-m long). 22
2.13. Experimental setup: optical fiber in a water tank at low depth. 23
2.14. Experimental setup: optical fibers in a 5-m depth water tank with a configuration closer to our end use. 23
2.15. (Right) Spectrogram of the signal in response to the chirp emitted by a buzzer under-water. (Left) SNR related to the signal, with a maximum peak of 30 dB. 24
2.16. Experimental results: (Top) Event count showing the pattern of the bit sequences transmitted by the router; (Bottom) The corresponding spectrogram. 24
2.17. Signal obtained due to latency limitations. 25
2.18. Quantum efficiency as a function of wavelength. 26
2.19. Overall steps for data processing and source position estimation. 26
2.20. Setup with the three fibers for localization. 27
2.21. Scheme related to experimental tests to locate the sound impacts created in a table. 27
2.22. Method to choose the K-value based on the ”elbow” criterion. 28
2.23. Dispersion between the three delays for each position studied. 28
2.24. Acoustic source localization using the validation dataset, with a maximum error of 49 cm and mean error of 17.9 cm. 29
2.25. Localization solutions according to the fiber configuration. 30
2.26. Dispersion between the delays and distance differences. 30
2.27. Physics-based model results yielding a mean error of 15 cm. 31
2.28. Timestamp of the signal start in the three fibers. 32

3.1. Polarization states mapped in the Poincaré sphere. 35
3.2. Types of deformations applied on the fiber 36
3.3. Polarization-based sensing for geology studies, namely for seismic monitoring. 37

3.4. Experimental setup for polarization-based acoustic sensing. 38
3.5. Frequency response to a chirp up to 10 kHz with the sensing fiber submerged in water. 39
3.6. Acquisition data and processing for objects classification procedure. 41
3.7. Experimental setup for the simplified interrogation scheme, using a polarization splitter to monitor orthogonal polarization components. 42
3.8. Second setup scheme: (POL) polarizer; (OBJ) objective; (PD) photodetector; (BS) beam splitter; (QW) quarter-wave plate; (F) optical fiber. 43

4.1. Multimodal sensing workflow for simultaneous acquisition and processing of polarimeter and EVS data. 45
4.2. Experimental setup for the multimodal sensing approach. 46
4.3. Localization error map: (a) using the dataset of 8 points: mean error of 21.8 cm and maximum error of 45.5 cm; (b) using the dataset with 43 points, used for training classification: mean error of 17.8 cm and maximum of 54.7 cm. 48
4.4. Confusion Matrix regarding classification of validation dataset. 48

5.1. Illustration of the capabilities of our final setup regarding 3D location and classification in real underwater environments (Adapted from [75]). 51
5.2. Overview of the sensing approaches investigated in this work and the main directions for future development. 52

List of Abbreviations

3D three dimensions. 3, 30

AUV Autonomous Underwater Vehicles. 3, 41, 52

CCD charge-coupled device. 10, 11

CMOS complementary Metal-Oxide semiconductor. 10, 11

DAQ Data Acquisition System. 18, 23

DAS Distributed Acoustic Sensing. 3, 7

DOP Degree of Polarization. 35

EMI Electromagnetic Interference. 2, 3

EVS Event-based Vision Sensors. 8, 12, 14, 45, 47

FBG Fiber Bragg Gratings. 4, 22, 37

FPI Fabry–Pérot Interferometers. 4

IMU Inertial Measurement Units. 2

KNN K-Nearest Neighbors. 27, 29, 33, 40, 44, 47, 50

LiDAR Light Detection and Ranging. 2, 3

MMF Multimode Optical Fiber. 5

POF Plastic Optical Fiber. 20

PSD Power Spectral Density. 19

PZT piezoelectric transducer. 18, 19, 22

ROI Region of Interest. 16, 17, 33

ROV Remotely Operated Vehicles. 3, 41

SLAM Simultaneous Localization and Mapping. 15

SNR Signal-to-Noise Ratio. 19, 23, 33, 39, 50

SONAR Sound Navigation And Ranging. 2

SoP State of Polarization. 35, 36, 39– 44, 46, 50

1. Introduction

It is hard to deny that the ability to perceive and interpret the surrounding environment is becoming increasingly important in the world of engineering and robotics. This fact motivates the continuous development of new sensing technologies, that aim to surpass current limitations and provide competitive advantages to enable operations in the most diverse real-world environments.

The selection of the sensors to be implemented for an accurate robot's perception highly depends on the operating environment and its complexity, and in many cases, the information obtained from using multiple sensors surpasses the simplicity of implementing a single sensing modality. This is particularly important in underwater environments, often characterized by harsh conditions, low visibility at high depths, and severe optical scattering and absorption. In these subterranean aquatic domains, light and electromagnetic waves attenuate rapidly within meters, making acoustic wave propagation the most effective physical mechanism for long-range underwater sensing, navigation, and communication. Moreover, recent advances in underwater applications, including offshore infrastructure monitoring [1], maritime security [2], environmental observation [3], and seismology studies [4], clearly point at an increase of the demand for compact and real-time **acoustic sensing systems**, indispensable for the study of vector sound field or acoustic imaging.

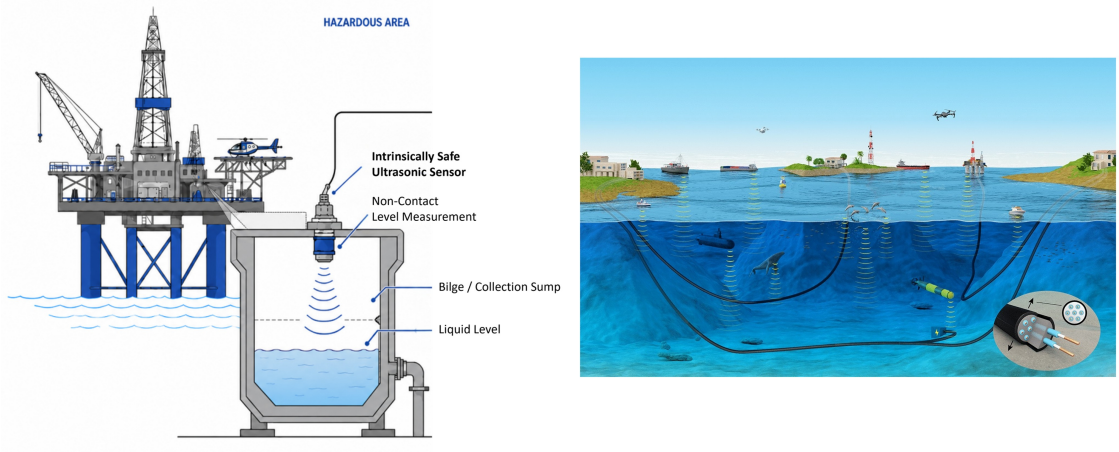

Figure 1.1: Examples of sensors implemented underwater: (Left) Ultrasonic sensors used in offshore monitoring applications; (Right) Acoustic sensors used for maritime security and environmental observation (Adapted from [5, 6]).

From a technological standpoint, conventional underwater acoustic detection predominantly relies on electronic transducers, such as piezoelectric hydrophones. Although

widely deployed, these systems are frequently constrained by bulky form factors, elevated fabrication costs, narrow operational bandwidths, and susceptibility to Electromagnetic Interference (EMI). To overcome these physical bottlenecks, optical fiber sensors have emerged as a highly promising alternative, offering intrinsic EMI immunity, miniature cross-sections, exceptional corrosion resistance, and high structural robustness in harsh subsea conditions.

Consequently, engineering compact, broadband, and resilient passive acoustic sensing architectures based on optical fiber platforms remains an interesting topic of research in underwater robotics, as existing fiber-based configurations continue to exhibit distinct trade-offs in terms of dynamic range, mechanical stability, or interrogation complexity. Addressing these fundamental limitations defines the core motivation for this thesis, where a novel optical sensing paradigm will be explored, using speckle pattern analysis and bypassing traditional interferometric constraints while achieving unprecedented temporal resolution through the integration of an **event-based camera**.

1.1. Proprioceptive and Exteroceptive sensors for robotics

In the context of robotics, sensors can be grouped into proprioceptive or exteroceptive modalities. Proprioceptive sensors measure the system's internal state. Examples include wheel encoders and heading sensors like gyroscopes and compasses, which are used to measure robot's orientation and inclination from the direction of a magnetic field. Inertial Measurement Units (IMU), are also common and typically include an acceleration sensor and a gyroscope, used for motion estimation [7]. Exteroceptive sensors, on the other hand, encompass all external sensors responsible for robot perception, localization, and environmental measurements. Positioning can be achieved through ground-based beacons like GPS, while motion and velocity estimation can be achieved with Doppler-based techniques. For more accurate analysis and decisions, vision-based sensors can provide richer information with other sensing modalities. Active ranging, based on time-of-flight (ToF) measurements, is also widely used in this domain. Examples include Sound Navigation And Ranging (SONAR) and as Light Detection and Ranging (LiDAR) systems, which estimate distances from the time delay between the transmitted and the reflected signals.

When available, optical sensing solutions are particularly interesting for their high spatial resolution, rapid data acquisition rates, and accuracy in terrestrial and controlled environments. Nevertheless, as previously stated, the performance of optical sensors is highly

dependent on the propagation dynamics of light itself, becoming particularly challenging in underwater applications: electromagnetic waves suffer from fast attenuation, while optical sensing is affected by scattering and turbidity-induced noise in water. As a result, sensors such as LiDAR or cameras are not as effective due to the low light conditions at high depths, making applications like stereo and three dimensions (3D) reconstruction more difficult [8]. Therefore, perception and navigation in most current Remotely Operated Vehicles (ROV) and Autonomous Underwater Vehicles (AUV) rely primarily on acoustic sensing technologies that present favorable underwater propagation characteristics with relatively low attenuation compared to electromagnetic waves, making them more robust in challenging environments for communication, location, and environmental perception applications.

1.1.1 Acoustic Sensing and optical fiber alternatives

Among acoustic sensors, the hydrophone is one of the most widely used in robotics, which, in short is an underwater microphone that converts pressure variations caused by sound waves into electrical signals for further analysis. When arranged in arrays, hydrophones enable not only sound pressure measurements but also directional information without left-right ambiguity, improving source localization [9]. Despite their widespread use, conventional electronic acoustic sensors present some limitations due to their susceptibility to EMI, their footprint, the need for electrical wiring, and cost (especially for ultrasonic-capable units), which may increase the system complexity and limit scalability.

In this context, optical fiber sensors present an interesting alternative to electronic devices, allowing to probe changes in the environment while presenting advantages like multiplexing capability, compactness, high sensitivity, and immunity to EMI. Based on their sensing approach, optical fibers acoustic sensors can be broadly divided into three main groups: **single-point**, **quasi-distributed** and **Distributed Acoustic Sensing (DAS)**. Starting from the latter, DAS systems rely on scattering phenomena - Raman, Brillouin, or Rayleigh backscattering ([10, 11]) - that occur in the entire fiber, analyzing the time delay between the transmitted signal and the arrival of the reflected one. This approach has opened many doors in underwater applications using seafloor optical fiber cables already installed from the optical communication network infrastructure [12, 13]; however, DAS systems generally contain expensive interrogation units and present a trade-off between spatial resolution, acquisition bandwidth, signal to noise ratio, and cost.

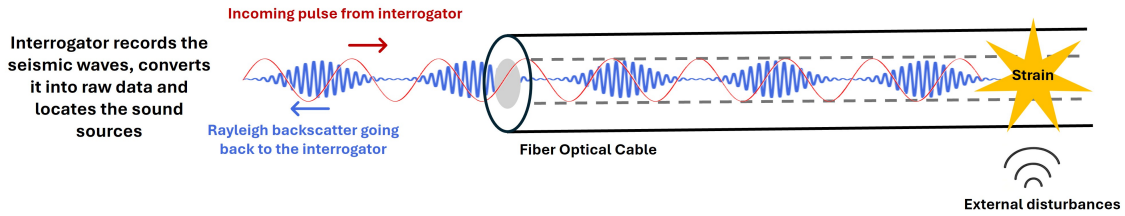

Figure 1.2: DAS interrogation scheme (Adapted from [14]).

More affordable, point-type sensors detect signals at localized points, providing high precision at specific positions. **Interferometric configurations**, for instance Mach-Zehnder [15], Michelson [16], Sagnac [17, 18], and Fabry–Pérot Interferometers (FPI) [19, 20], are particular choices for acoustic sensing applications, due to their high sensitivity and long sensing distance. However, due to their intensity-based detection approach, are sensitive to environmental disturbances like temperature, light power fluctuations, and mechanical drift. Additionally, some interferometric configurations require delicate optical structures, increasing their complexity and fragility at great depths, and the spatial resolution is far from ideal.

Fiber Bragg Gratings (FBG) - wavelength-based point-type sensors - present an alternative solution, exploring the reflection of particular wavelengths of light that depend on the refractive index (n_{eff}) or grating period of the fiber grating (Λ): $\lambda_b = 2n_{eff}\Lambda$ [21]. They are easier to multiplex than interferometric sensors, meaning that many FBG can be placed in the same fiber. In recent years, new methods for acoustic sensing have been proposed using FBGs, such as diaphragm-based optical fiber sensors [22], where acoustic pressure deforms a diaphragm producing variations in the optical path length (commonly in FPI structures). Additionally, resonant-based sensors have gained attention consisting of a sensing structure fabricated at the fiber tip, where the resonance wavelength of a micro-ring changes in response to external stimuli ([23], [24], [25]), opening doors for applications like photoacoustic tomography. Notwithstanding these points, each FBG must operate at a distinct Bragg wavelength, and the need of direct inscription into the fiber makes the manufacturing costly and the interrogation slower, which is critical if the objective is to interrogate many points along the fiber. Fused-tapered optical fiber coupler sensors have also been already explored [26] although it also has limitations in terms of fragility and sensitivity to environmental fluctuations.

Addressing the aforementioned limitations and providing a sensing solution that is compact, cost-effective and easy to interrogate, **speckle-based optical fiber sensors** have

recently emerged as a promising alternative. Speckle pattern phenomena was discovered in the early 1960s with the development of the laser: when laser light was reflected from a surface and a fine-scale granular pattern was observed. From the underlying physics, it can arise from two different mechanisms (Fig.1.3). One mechanism is caused by the interference of dephased wavelets scattered by rough optical surfaces. The resulting random speckle pattern encodes information about the object's deformation, enabling the development of a wide range of methods, such as speckle photography and speckle shear interferometry [27]. Speckle is also an important concept for cases like Synthetic Aperture Radar Imagery, to study Earth, or for ultrasound medical imagery [28].

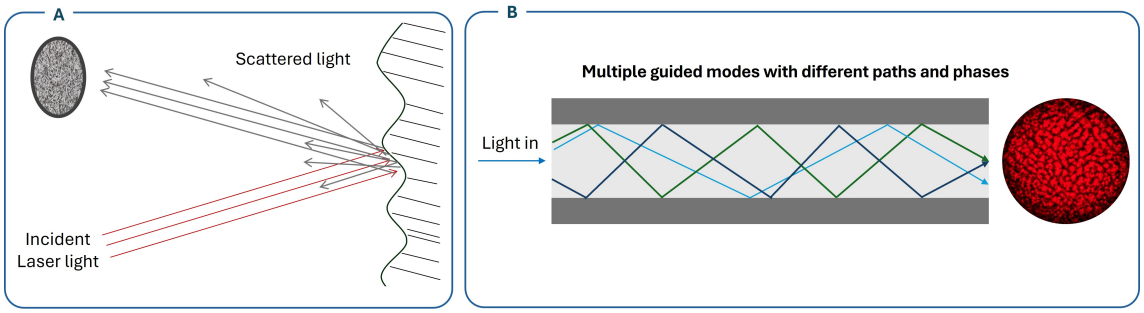

Figure 1.3: Physical mechanisms underlying speckle pattern formation: (A) generated on light scattering from rough optical surfaces; (B) generated by modal interference in optical fibers.

The second mechanism, which is the highlight of this work, is related to the formation of speckle from the interference of guided modes propagating a multimode optical fiber where its contrast increases as the light source bandwidth decreases [29]. The first studies on fiber speckles appeared in the 1970s, marked by several works reporting the observation of speckle patterns at the output of multimode fibers. These were soon followed by the first acoustic sensors based on intermodal interference in 1977 [30]. Since then, Fiber Specklegram Sensors (FSSs) have attracted increasing interest for a wide range of sensing applications, including for bending and curvature measurements [31], tactile sensing, biomedical monitoring [32], and intrusion detection. More recently, machine learning techniques such as AlexNet, VGGNet, and ResNet have also been employed to improve the interpretation and classification of speckle patterns.

To further understand the dynamics of the speckle pattern and how they depend on the environment, we may start by introducing a simplified mathematical model. When spatially coherent light is launched into a Multimode Optical Fiber (MMF), multiple guided modes are simultaneously excited. Each one is characterized by its electric field distribution

$E(r,\phi)$, and a propagation constant, $\beta_m = n_1 k_0 cos(\theta_m)$ that must satisfy the boundary condition at the core-cladding interface to remain confined in the fiber core [33]:

$$\frac{2\pi n_2}{\lambda_0} < \beta_m < \frac{2\pi n_1}{\lambda_0} \tag{1.1}$$

where n_1 and n_2 are the refractive indices of the core and the cladding, respectively, and λ_0 is the optical wavelength. The optical field propagating inside the fiber can be expressed as the superposition of all excited modes:

$$E(r,\phi,z) = \sum_{m=1}^{M} A_m E_m(r,\phi) e^{-j\beta_m z} \tag{1.2}$$

where A_m represents the excitation coefficient of the m-th mode and M is the total number of guided modes.The variables *r, ϕ* and *z* denote the radial, azimuthal and propagation directions, respectively. Low-order modes are strongly confined within the fiber core and the fundamental mode has an approximately Gaussian profile in contrast to higher-order modes which are characterized by more complex transverse intensity profiles and are associated with a decrease of beam quality [34]. Although most of the optical power remains confined within the core, a small part of it penetrates into the cladding region, contributing to the evanescent field which decays exponentially with the distance from the core-cladding interface. The distance at which the field amplitude decreases to $1/e$ of its value at the interface, is known as the penetration depth, given by:

$$d_p = \frac{\lambda_0}{2\pi\sqrt{n_1^2 sin^2\theta_m - n_2^2}} \tag{1.3}$$

At the fiber output, the interference of guided propagation modes with different phases accumulated along the fiber length generates what we call the **speckle pattern**. Constructive and destructive interference between the modal fields generates a granular intensity distribution that is highly dependent on the relative phases of the propagating modes. Using our model, the light intensity at the output of the fiber with length L can be written as:

$$I(r,\phi) = \left| \sum_{m=1}^{M} A_m E_m(r,\phi) e^{-j(\beta_m L - \phi_m)} \right|^2. \tag{1.4}$$

Expanding, we get:

$$I(r,\phi) = \sum_{k=1}^{M} (A_k)^2 \Big(E_k(r,\phi)\Big)^2 + 2\sum_{i=2}^{M}\sum_{k=1}^{i-1} A_k A_i E_k(r,\phi) E_i(r,\phi) cos[\Delta\beta_{ik} L + \Delta\phi_{i,k}], \tag{1.5}$$

where A_i is the amplitude of the i-th mode; $E_i(r,\phi)$ is the mode field distribution; $\Delta\beta_{ik} =$

$\beta_i - \beta_k$ is the difference in propagation constants, and $\Delta\phi_{ik} = \phi_i - \phi_k$ is the phase shift difference, usually random. The first term is a constant component, while the second term is related to the sum of interferences of the excited modes [30].

For sensing applications, the key point is that the speckle pattern is extremely sensitive to external perturbations such as strain, bending, pressure, temperature variations, or acoustic waves from the surrounding environment: these may induce both phase deviations and mode coupling, where the energy is transferred between the different propagation modes [35]. Consequently, these perturbations cause the speckle pattern to vary over time and, by monitoring the temporal evolution of the speckle intensity, acoustic signals can be detected and characterized (Fig. 1.4).

Compared to the aforementioned acoustic fiber-optic sensing technologies, speckle-based sensors do not need complex microfabrication such as gratings or interferometric cavities, relying only on multimode interference and image acquisition. Besides, as each location leads to distinct variations on speckle pattern, speckle-based optical fiber sensors may also work as a distributed or quasi-distributed sensing strategy [36], in the sense that both provide information about perturbations along the sensing fiber, but its interrogation scheme is simpler than conventional DAS systems. This makes them a highly valuable solution for applications in underwater robotics, thanks to their simplicity, compactness, cost-effectiveness, and low computational load, not to mention their extreme sensitivity to small perturbations.

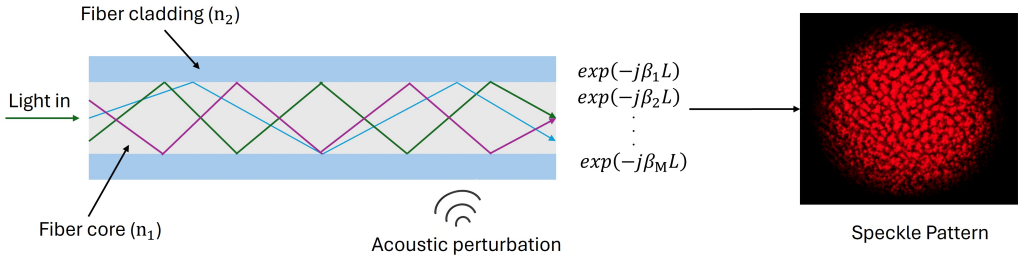

Figure 1.4: Speckle interrogation scheme: propagation of M modes in the fiber.

Finally, we shall also mention that multisensor fusion may be utilized to give richer information than a single sensing modality alone. Although it is an emergent area of research, one can argue that further information such as polarization state can also be utilized for enhancing acoustic sensing. Indeed, polarization-based strategies have already been used in large-scale applications such as locating and monitoring seismic waves, by interrogating the polarization state in spatially distant repeaters, susceptible to changes due

to external perturbations, as seen on the article of Luis Costa et. al [37]. Besides, polarization information fusion has already been explored in new applications of computer vision and robotics, particularly on the topic of passive polarization vision in autonomous vehicles, namely the integration of polarization sensors on board robots [38]. Some implementations are bio-inspired approaches motivated by animal behaviors, allowing the exploration of polarization imaging in aviation, to enhance guidance systems under challenging and low-visibility conditions [39, 40].

1.2. Objectives and thesis structure

The limitations of the conventional acoustic sensors presented, especially in underwater harsh environments suggest the need for alternative approaches that combine robustness, sensitivity, and simplicity. Optical fiber-based sensors cover some of those questions as argued, however, some approaches rely on complex interrogation schemes. Emerging speckle-based techniques, appear as an interesting solution due to their simplicity and high sensitivity, but conventional frame-based imaging interrogation introduces **data redundancy** and **limited temporal resolution**. Recent innovations in event-based (neuromorphic) cameras suggest a promising alternative to the traditional imaging systems for speckle interrogation [41], yet their application to fiber-based solutions and, in particular, to underwater environments remains to be explored.

This introduces the main objective of this thesis, which focuses on investigating and developing an acoustic sensing system based on optical fiber sensors, interrogated using Event-based Vision Sensors (EVS) [42, 43], aiming to improve performance in challenging underwater environments, by offering a **low-cost** and **high-resolution solution**, and also the capability of **scalability** by monitoring multiple fibers within the same field of view simultaneously. In specific, the work consists of four main operational objectives:

1. To characterize the frequency response of a speckle-based sensor in air and also underwater, in conditions closer to our final use, using EVS for interrogation;
2. To evaluate the capability of the system to perform source localization;
3. To develop a polarization-based sensing system to complement the information, for instance, enabling acoustic source classification;
4. To implement a multimodal sensing system that integrates both functionalities from an EVS and a polarimeter, compensating for each other's limitations.

To cover these objectives, the present thesis is organized in five chapters. The first chapter motivates the present work and provides a brief introduction of fiber-based acoustic sensing systems, exploring in particular speckle sensing and its unique advantages for the current goal of this work. Building on the need for a faster interrogation strategy, the second chapter explores the key advantages of event-based cameras for interrogating speckle sensors and characterizes the fiber sensor frequency response in both air and underwater environments, under conditions closer to the sensor's final use. This chapter also presents the evaluation of the system for surface-based localization, through two distinct methods. Then, moving to multimodality to increase the bandwidth of the system, the third chapter explores a polarization-based sensing system, which provides additional information that can be used, for instance, for event classification. This is validated with the preliminary results presented in the fourth chapter, which deals with the fusion between the speckle and polarization sensing modalities, with the objective of improving the sensing performance and being able to do simultaneously localization and classification of a given event. Finally, Chapter 5 wraps up the work, presenting an additional discussion on perspectives for future work.

1.3. Thesis outputs

Oral presentations:

- ”Acoustic Detection and Source Localization with Event-Based Fiber Speckle Sensing”, **Sofia Duarte**, Joana Teixeira, Tomás Lopes, Nuno A. Silva, Catarina S. Monteiro, AOP Lisbon - 7th International Conference on Applications of Optics and Photonics, (2026)

Poster presentations:

- ”Acoustic Detection and Source Localization with Event-Based Fiber Speckle Sensing”, **Sofia Duarte**, Joana Teixeira, Tomás Lopes, Nuno A. Silva, Catarina S. Monteiro, EPS Young Minds Porto, (2026)

Conference Proceeding:

- ”Low-SWaP Optical Fiber Acoustic Sensor for Underwater Vehicles with Event-Based Interrogation”, **Sofia Duarte**, Tomás Lopes, Joana Teixeira, Tiago D. Ferreira, Bruno Matias, Carlos Almeida, Nuno A. Silva, Catarina S. Monteiro, Proceedings of SPIE Security + Defence, (2026)

2. Event-based Vision for Speckle Interrogation

As introduced in the previous chapter, speckle patterns are generated after multimode interference within the optical fiber and interrogated using imaging sensors, allowing the detection of perturbations [44]. Variations in the physical conditions to which the fiber is exposed modify the relative phase and amplitude of the propagating modes, resulting in changes in the spatial distribution of the output speckle pattern. Therefore, the use of speckle patterns as a sensing mechanism requires the acquisition and analysis of their temporal evolution, which is conventionally performed using imaging cameras.

The most common approach for speckle-pattern interrogation relies on conventional frame-based imaging technologies, particularly charge-coupled device (CCD) and complementary Metal-Oxide semiconductor (CMOS) cameras. Several speckle-based sensing applications employing these devices have been reported in the literature, including the measurement of physical quantities such as stress, temperature, displacement, vibration, magnetic field, and refractive index. These sensing approaches have been investigated across a wide range of application domains, including astrophysics [45]. Although most reported systems employ commercially available MMF, specialty fibers and specifically fabricated structures have also been investigated to enhance the sensitivity of speckle-based sensing systems. One example is the use of tapered multimode fibers, in which the reduction of the fiber diameter increases the interaction between the guided modes and the surrounding medium through the evanescent field. Consequently, variations in the refractive index of the external medium modify the effective refractive indices of the propagating modes. This alters their relative phase and, therefore, the modal interference observed at the fiber output. As a result, different surrounding refractive-index values produce distinct speckle patterns, allowing refractive-index variations to be detected through the analysis of the spatial intensity distribution [46].

Another relevant application of fiber speckle sensing is the monitoring of geophysical phenomena, particularly seismic activity. In a recent work [47], the speckle pattern produced by a multimode optical fiber was acquired using a CCD camera operating at 30 frames per second (fps), and vibration components with frequencies of up to 10 Hz were successfully detected. The study investigated the feasibility of using fiber-optic speckle sensing for earthquake detection and compared the proposed approach with conventional seismic

instrumentation. In particular, the Geophysical Institute of Ecuador employs tri-axial seismometers containing three sensing elements and capable of detecting ground vibrations over a frequency range from approximately 0.03 Hz to 50 Hz. To analyze the speckle, a technique of averaged difference was used, which allows obtaining intensity variations of 2 consecutive frames, and a Moving Average filter was applied to reduce the noise. The random movement generator of the speckle pattern was characterized by frequency values given by the roots of a quadratic equation, whose coefficients were taken from the polynomial fit $Y = a + bf + cf^2$, where Y is the mean intensity value. With that, the proposed system was able to detect random movements similar to P and S earthquakes waves.

2.1. From image to event-based vision

Briefly, the working principle of a regular camera sensor is to capture the intensity of light hitting the sensor; the higher the intensity, the greater the accumulated charge. In the CCD sensor, each charge is transferred from pixel to pixel before being converted into a voltage, whereas in a CMOS sensor, each pixel does its own digitization, requiring less power. By reading the volume of light that accumulates in a pixel, CMOS sensors also count the noise that enters along with the photons, contaminating the information. These cameras capture an entire image using a frame-based approach, meaning the sensor is integrating the field of view over a fixed time interval (exposure time) at a pre-assigned interval (framerate), whether changes occur or not, resulting in significant data redundancy. A regular camera outputs a matrix of pixels `(t,F)` with the respective intensity (`F`) at a certain timestamp (`t`) - synchronously-, i.e. a set of intensity values is measured at the same time, producing an image frame nearly simultaneously.

Since all pixels are read simultaneously, the resulting measurements provide a synchronous representation of the scene. However, when applied to speckle-based sensors, this translates into a few limitations on the interrogation side. First, their temporal resolution is fundamentally constrained by the frame rate, reaching typical values of a few hundreds of Hz with reduced regions of interest (e.g. 50-250 fps). Rapid variations occurring between consecutive frames may therefore be undersampled or completely missed, limiting the maximum frequency and transient dynamics that can be reliably characterized. Increasing the frame rate can partially mitigate this limitation but generally results in substantially larger data rates. Indeed, frame-based cameras acquire the intensity value of every pixel at every acquisition instant, regardless of whether a significant change has occurred in

the corresponding region of the image. Speckle sensing consequently generates large volumes of highly redundant image data, particularly during periods in which the system is in a stationary or quasi-stationary state. Processing these full-frame sequences requires considerable memory bandwidth, storage capacity, and computational resources for operations such as frame differencing, filtering, correlation, or feature extraction. Additionally, sensor noise, illumination fluctuations, mechanical drift, and other small intensity variations can produce measurable differences between consecutive frames even in the absence of a relevant external perturbation, potentially increasing the complexity of distinguishing meaningful events from background fluctuations.

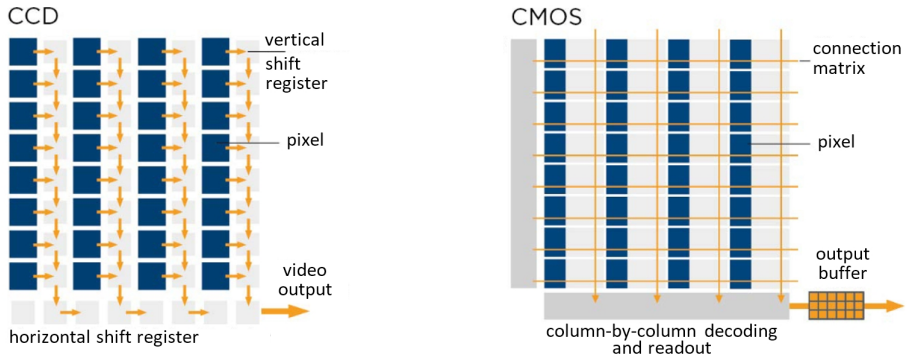

Figure 2.1: CCD and CMOS operating principles [48].

To overcome the limitations of this hardware, **neuromorphic vision systems** have emerged as a promising approach, using bio-inspired sensors designed to mimic the human eye [49]. Similarly to how the retina captures light and translates it into nerve impulses the brain can interpret, a sensor captures light passing through a lens and converts it into electric signals that are then processed and digitized into an image. Instead of capturing pixels within a field of view, the main data points generated in this system are **events** - the core unit of information in EVS. An event is a single-pixel detection of brightness, contrast changes, or movement, which are described by $\{t, X, Y, p\}$, where the timestamp (t) is the time the change occurred, X and Y are the horizontal and vertical coordinates on the sensor where the change occurred, respectively, and the polarity (p) is the sign of the change: Positive (+1) or negative (-1) if it represents an increase or decrease in intensity, respectively.

This asynchronous operation helps minimize the volume of processed data by independently triggering events at each pixel whenever a change in intensity exceeds a predefined threshold. Additionally, EVS offer **high temporal resolution**, related to the accuracy of the clock readout circuit, i.e., the minimum time span between two events in distinct pixels,

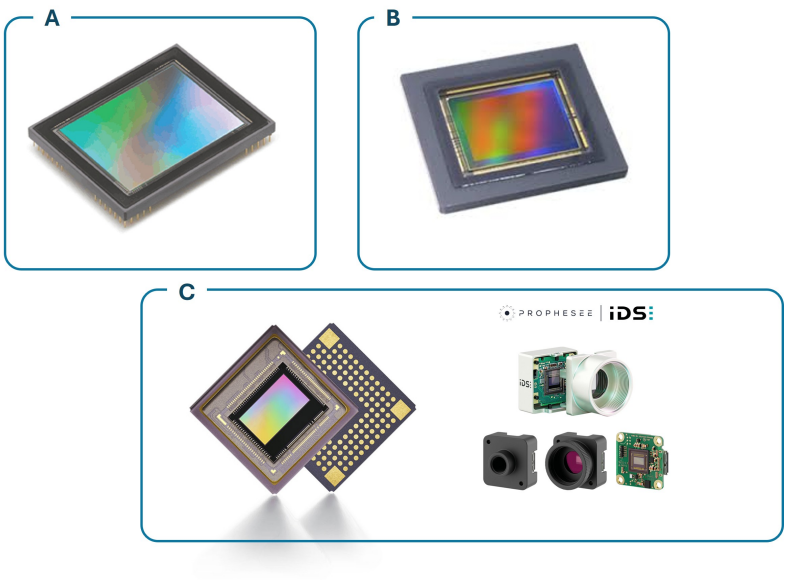

Figure 2.2: (A) CCD sensor; (B) CMOS sensor; (C) Event-based camera (Adapted from [50, 51]).

that can reach 1 μs. Thanks to this, it is possible to visualize high-frequency movements, such as vibrations and acoustic signals. The **latency**, by definition, the time between an input and the respective output or the delay between the occurrence of an event and its observation on the screen, goes from milliseconds to microseconds in one case to another, allowing for near-continuous tracking of scenes in real time. This translates into equivalent high frame rates of up to 10.000 fps, while high-quality commercial cameras achieve a typical maximum of 120 frames per second. In addition, it enables an event output with a **high dynamic range** ($>$ 120 dB).

These properties opened new perspectives on applications in the industrial field due to the high precision and efficiency of movement records. We are talking about high-speed and high sensor resolution, able to detect fast moving objects or people, equipment monitoring, image analysis, and recognition. Moreover, by ignoring uniform stimulus, the amount of data is reduced as well as the motion blur or the lack of detail. Conventional cameras, by capturing large amounts of irrelevant information (at stationary scenes), consume unneeded bandwidth, with a fixed framerate, and can lose some important data and make it difficult to obtain a clear image without distortion in situations of moving objects.

Taking into account this innovative way of interrogation in relation to conventional cameras, speckle patterns generated by acoustic signals can be identified and the intensity changes in each pixel due to variations of pressure and deformations in the optical fiber can lead to the reconstruction of those signals:

$$\frac{\delta}{\left|\frac{\partial I}{\partial \delta}\right|} = \left[I(\delta) - I_0\right] \Leftrightarrow \delta = \left[I(\delta) - I_0\right] \cdot (\partial_\delta I)^+ \tag{2.1}$$

where the term $I(\delta) - I_0$ is related to the speckle intensity variation with respect to the applied stimulus, δ.

In the EVS, in each pixel the incident light is converted into electric signals through a photodiode and a I/V converter responsible for conversion of current into voltage. The next step on the luminance change detection unit consists of a differential detection circuit based on Delta Modulation that detects the changes between the reference voltage and the converted incident light voltage, and a comparator circuit that generates an event and outputs the data if the delta exceeds either plus or minus thresholds (figure 2.3).

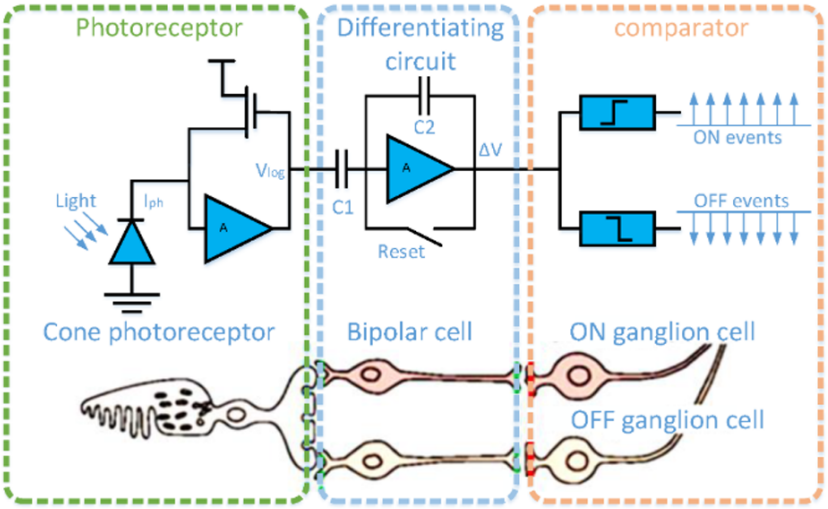

Figure 2.3: Similarities of working principles between human eye and EVS [52].

The circuit is reset as the event luminance is detected (if it surpasses or goes lower than the positive or negative thresholds, respectively) and stablish it as the new reference voltage. The threshold values are also set from this new reference: in the positive (light) or negative (dark) directions, and so on. The event triggering condition is given by

$$C(t) \leq \log I(x,y,t) - \log I(x,y,t_p), \tag{2.2}$$

where $I(x,y,t)$ is the light intensity of the pixel (x,y) at time t, and $I(x,y,t_p)$ is the intensity at the instant of the previous event generated by the same pixel, t_p. The fact that the conversion into electric voltage is in a logarithmic scale makes it possible to detect small

differences in the low luminance range and respond to a wide difference in the high luminance range, preventing saturation. This explains the higher dynamic range mentioned before.

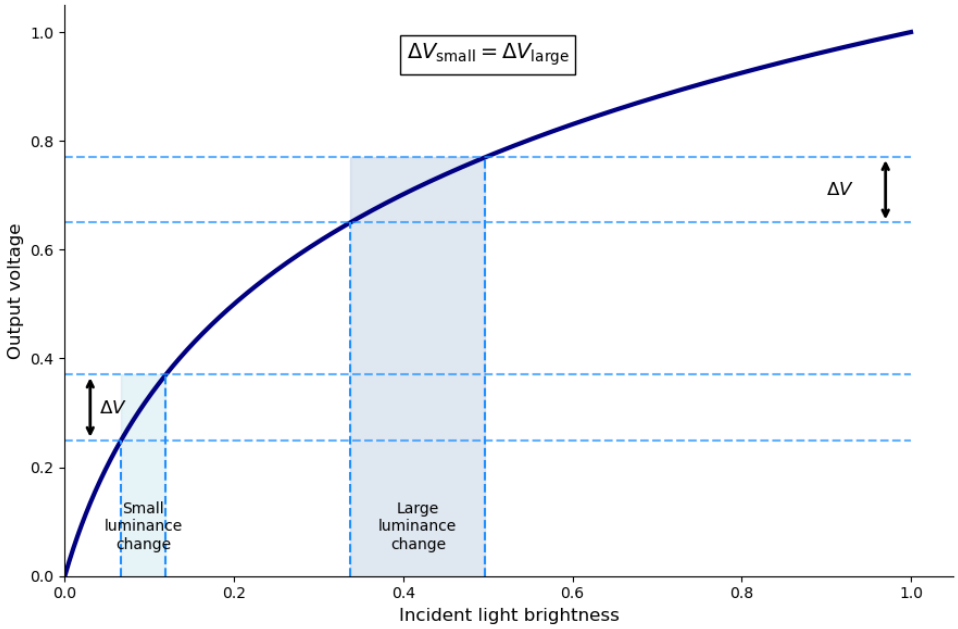

Figure 2.4: Relation between incident light luminance and output voltage on the pixel unit.

That being said, in addition to the applications mentioned previously that we will work on, event-based camera sensors are already revolutionizing other areas. Some examples are: **object detection** [53] and **tracking** [54], predicting a long-term trajectory for objects at high speed motion; **classification** [55] and **recognition** (e.g. action and gait recognition, human age classification); **visual odometry** [56] and **Simultaneous Localization and Mapping (SLAM)** [57]; **estimation**, including optical flow, which is a field described by displacement vectors, motion or depth estimation for event streams [58]; **Stereo Depth imaging** by predicting a disparity map given left and right event sequences [59]; **Reconstruction and image processing** applied in tasks such as event denoising and motion deblurring [60].

2.2. EVS: Data acquisition and processing

To capture the output speckle pattern, a Sony Prophesee IMX636-AAMR-C sensor (UE-39B0XCP-E) with approximately 0.92 M effective pixels was employed, featuring a resolution of 1280 $\times$ 720 and a pixel size of (4.86 $\times$ 4.86) μm [61]. This chip operates with analog 3.0 V, digital 1.1 V, and 1.8 V triple power supply. Software integration was performed using the Metavision SDK from Prophesee, which offers a wide range of functionalities

(Fig. 2.6): configuration of display settings such as accumulation time; setting a Region of Interest (ROI); controlling pixel biases, related to the minimum contrast to trigger an event; and configure event processing like Anti-Flicker, and Trigger interfaces. Noting that controlling those biases can be helpful by eliminating the noise, but also reduces in some way the range of signals detected.

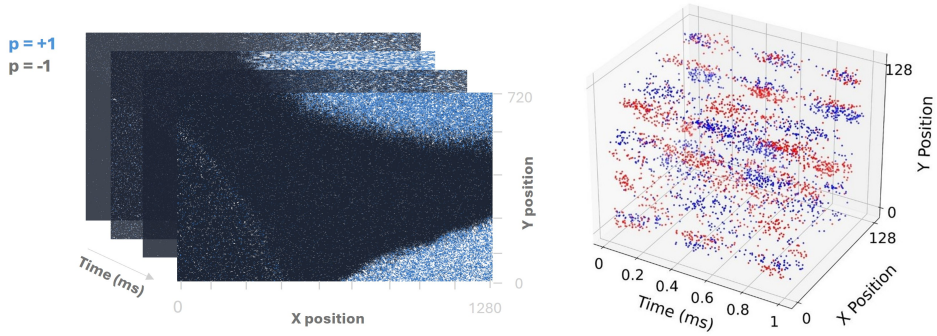

Figure 2.5: (Right) Spatial images obtained from the acquired event stream data (left).

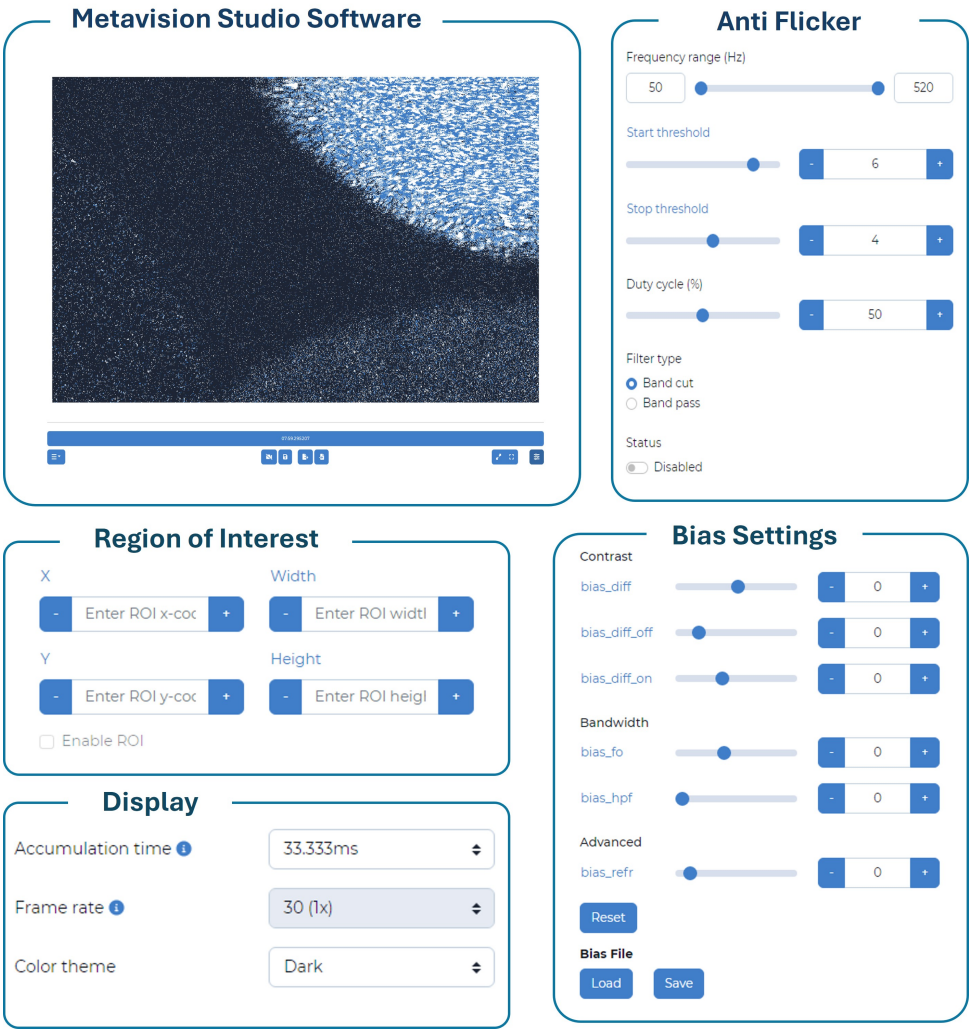

Figure 2.6: Metavision software overview: Anti-Flicker, ROI, Display and Bias settings.

Two different methods can be used for data recording. The first approach is executed in the Metavision software, where data files are generated containing the detected events stored according to their timestamp, pixel coordinates and polarity (`t,X,Y,p`). The second method relies on the Threads Module, generally used to overcome synchronization issues between input and output signals. In this approach, the data files can be generated directly within the Python environment by following the procedure:

1. Generate the excitation signal by concatenating, for instance, sinusoidal bursts or linear chirps;
2. Create a *Thread* responsible for playing the excitation signal through the acoustic source;
3. Create a second *Thread* to initialize the event-camera recording;
4. Start both *Threads* simultaneously to ensure synchronized acoustic excitation and event acquisition during a predefined acquisition time.

In both cases, the data files are generated in `.hdf5` format, and subsequently analyzed and processed, with the complete data processing workflow summarized in Fig. 2.8.

Following data acquisition, the recorded event stream is processed to reconstruct the temporal response of each sensing fiber. Initially, all detected events generated with the camera are stored according to their timestamp, pixel coordinates, and polarity, `(t,x,y,p)`. These events are then temporally integrated into a 2-dimensional frame by accumulating the number of detected events at each pixel position.

The first processing step consists of delimiting the spatial grid size for each fiber. This is achieved by selecting the ROI (`ROI_X` and `ROI_Y`), manually or automatically. In the automatic approach, a Gaussian filter is first applied to reduce noise and then a percentile-based threshold is used to identify the most active regions, assigning them then to a pre-selected number of bounding boxes, as illustrated in Fig. 2.7.

Using a pre-defined sampling time interval, Δt, it is possible to initialize a 2D array and accumulate event polarities within successive temporal windows. By continuously repeating this process for subsequent windows, a sequence of temporal intensity samples is created, from which the temporal intensity signal is reconstructed for each fiber. Having that, it is possible to compute the spectrograms and analyze the respective signals in the time-frequency domain.

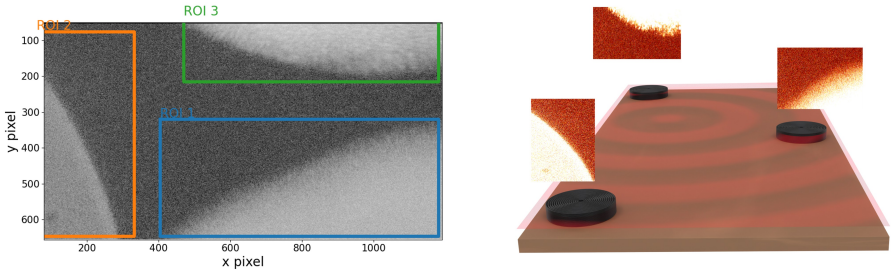

Figure 2.7: (Left) Detection of three ROIs automatically after the accumulation of the detected events. (Right) ROIs obtained for each output fiber.

For an appropriate ROIs selection, condition required to an accurate evaluation of the sensing channels, the speckle patterns must be sufficiently separated to avoid overlap between events, and all ROIs should have similar event intensities, which can be verified using a *ThorLabs' Zelux* RGB camera.

The following workflow (illustrated in Figure 2.8) is essential to evaluate the performance of experimental tests. To assess the sensing capabilities of the setup, a piezoelectric transducer (PZT) was mechanically coupled to the optical fiber. Electrical signals, which included single-frequency tones and chirp signals, were generated through a NI USB-6351 Data Acquisition System (DAQ) and applied to the PZT, inducing mechanical deformations in the fiber and, therefore, modifying modal interference and producing changes in the output speckle pattern.

The measured signal must be sampled at a sufficiently high rate to accurately capture the frequencies of the response and avoid aliasing. For that, the sampling frequency must be at least twice the maximum frequency of interest according to the **Nyquist-Shannon** sampling Theorem:

$$f_s \geq 2f_{max} \tag{2.3}$$

For the characterization of the fiber response to the tests that will be covered in the next section, additional metrics and functions were analyzed, the most important of which are:

1. Signal intensity as a function of time, to analyze the temporal response of the fiber to the applied signal;

2. Spectrograms, allowing the visualization of the frequency over time as well as the amplitude, through Fourier Transforms. The parameters *nperseg* and *noverlap* that

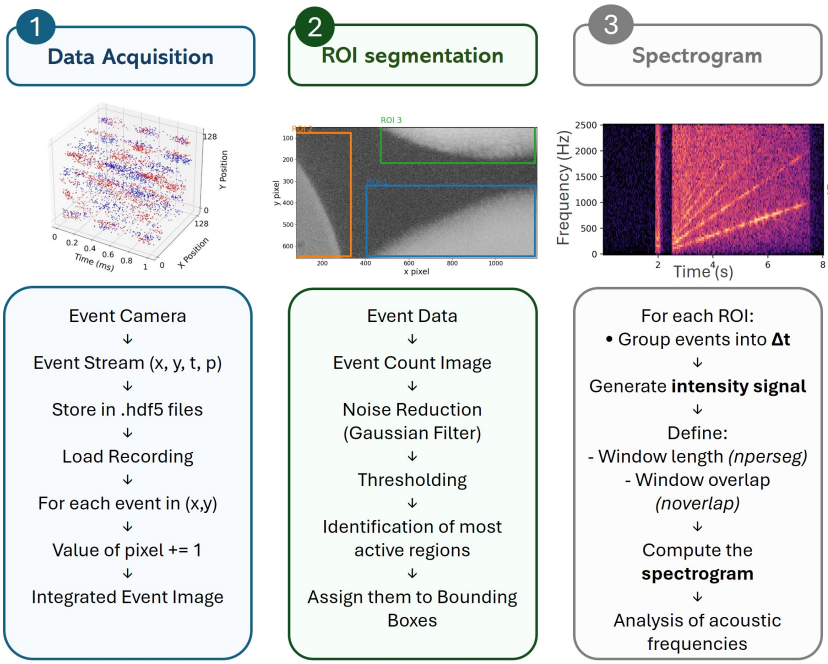

Figure 2.8: Overall steps for data acquisition and processing.

represent the segment length and the number of points to overlap between segments, respectively, need to be defined.

3. Power Spectral Density (PSD), to evaluate how the signal power is distributed across different frequencies;

4. Signal-to-Noise Ratio (SNR) as a function of frequencies. SNR is calculated by:

$$SNR = 10 \cdot log\left(\frac{P_{signal}(t)}{P_{noise}(t)}\right) \tag{2.4}$$

where $P_{\text{signal}}(t)$ is the signal power and $P_{\text{noise}}(t)$ is the average noise power. It can be obtained from the spectrogram by comparing the signal power around the applied signal frequency, which is a linear chirp and therefore it can be deducted for every instant, with the average noise power outside a predefined frequency margin (± 100 Hz as the frequency window in this case).

2.3. Signal Detection in air

To evaluate the performance and sensitivity of the optical fiber under acoustic excitation, several fiber configurations were tested both in air and water tanks, using PZT and loudspeakers as acoustic sources. The general experimental setup is shown in Figure 2.9, where the output speckle patterns of the fibers are aligned and projected onto the same

EVS, while linear polarization control is used to adjust and ensure an equalized optical power, improving the detected speckle response.

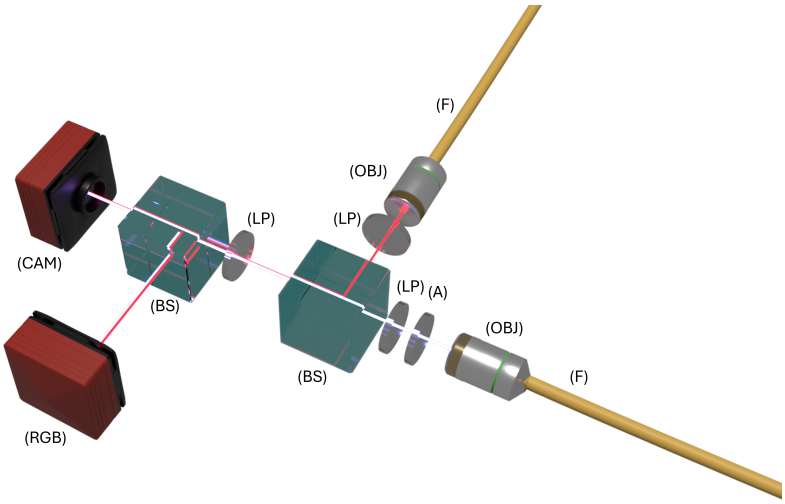

Figure 2.9: Setup of the event-based camera with 2 optical fibers. (A) Attenuator; (BS) Beam Splitter; (EVS) Event-based camera; (F) Optical Fiber; (O) Objective; (LP) Polarizer; (RGB) ThorLabs RGB camera.

Step-index multimode fibers with different core diameters were tested, namely 62 μm, 600 μm and 1 mm, to evaluate an eventual influence of the number of modes on the speckle response, which increases with the core radius, according to the V-number.

$$V = a\frac{2\pi}{\lambda}NA \tag{2.5}$$

where *a* is the core radius, *NA* is the numerical aperture, and λ is the laser wavelength.

The fibers were initially tested in air, where the 62 µm fiber only had satisfactory results when the coating was removed, making it more fragile, especially in harsh environments. The best overall results were obtained using 1 mm Plastic Optical Fiber (POF) wrapped in multiple loops rather than in a straight configuration. This can be justified by having more points along the fiber sensing the same deformation, making it more likely to detect a response to that perturbation. Another reason may have to do with the fact that the fiber's loops can act as a filter, allowing only the essential information to reach the output speckle, which is our source of analysis. To conduct the experimental tests, the fibers were placed on the table as shown in Fig. 2.10 and suspended in plastic containers, which seemed to act as mechanical amplifiers (Figure 2.12a).

POF are made of a fluorinated polymer, are cheaper, have a larger core diameter (varying from 50 μm to 3 mm), and have the main advantage over conventional silica fibers of being more resistant to bending and stretching [62], while other conditions remain the

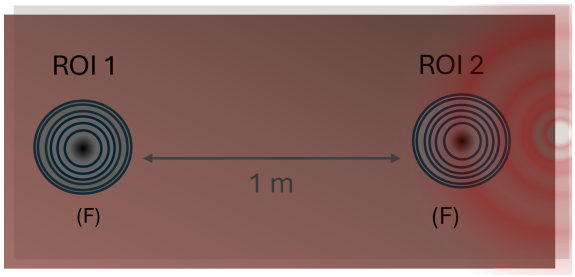

Figure 2.10: Illustration of 2 fibers for acoustic signal detection in air: (F) Optical Fibers.

same. This is particularly beneficial underwater, where sensing systems are frequently subjected to harsh conditions and mechanical stress.

Results In air, it was detected acoustic excitation in the fiber located closest to the acoustic source, corresponding to ROI 2, with a maximum SNR of 25 dB (Fig. 2.11), while ROI 1, about 1 m apart, achieved the highest SNR at frequencies below 600 Hz. The signal emitted was divided into a burst with a frequency of 250 Hz, followed by a chirp between 1 Hz and 1 kHz. Especially in ROI 2, it was possible to detect other harmonics besides the fundamental one, likely due to the nonlinear response of the acoustic source or the resonant frequencies of the plastic containers holding the fibers.

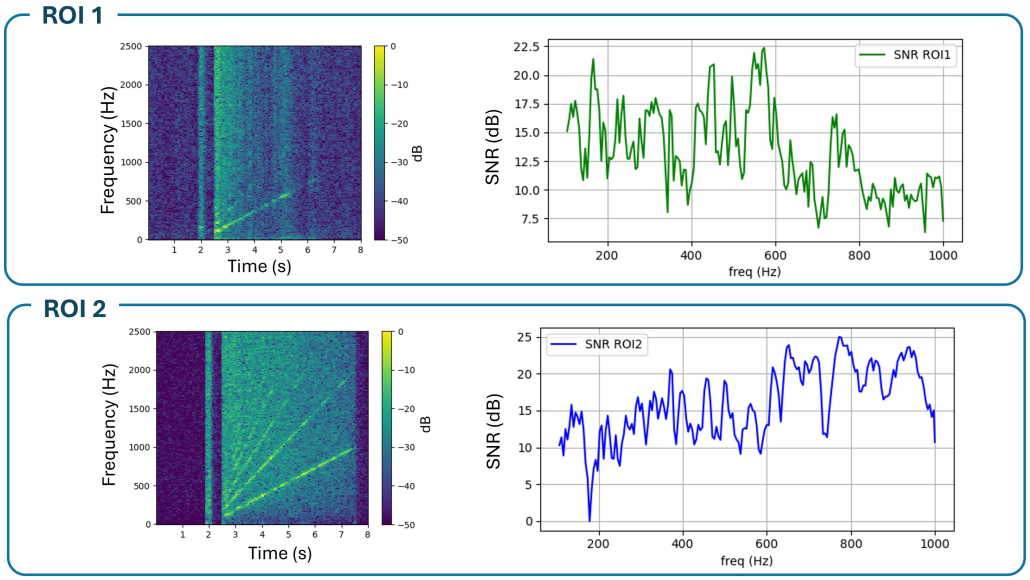

Figure 2.11: Spectrograms of the signal in air (left); SNR vs applied frequency (right).

Other configurations, besides the one involving plastic containers, were as follows:

1. Placing the fibers around a PVC pipe (Figure 2.12b).

2. Wounding approximately 15 meters of fiber (around 190 loops) around a cork mandrel (Figure 2.12c). This approach was inspired by compliant mandrel designs reported in the literature. Cork was selected due to its low Young's modulus and near-zero Poisson's ratio, allowing it to deform under pressure without significant axial elongation. This reduces mechanical stress on structural components while improving sensitivity to low-intensity acoustic signals [63].

3. Wounding approximately 15 meters of fiber around a rigid coil (Figure 2.12d), forming about 120 loops, and where radial deformations of the structure could induce strain in the fiber, influencing its response.

4. Another configuration involved placing the fiber on top of a thin plastic membrane, enabling the detection of mechanical vibrations, similar to approaches that have been successfully implemented using FBG sensors [64].

Despite these efforts, the results obtained were not sufficient. Possible reasons include malfunction or inadequate coupling of the PZT during the tests, or due to mode instability of the initial laser sources, also susceptible to temperature variations, which may mask the detection of the true signal. To address that limitation, the lasers were then replaced with blue and red single-mode lasers.

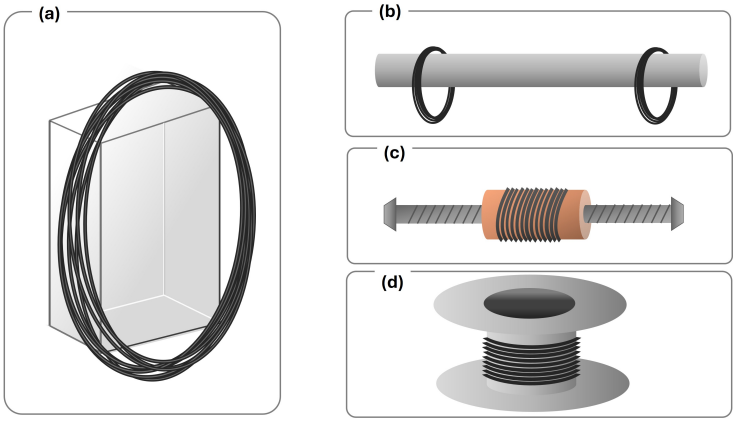

Figure 2.12: (a) Setup with plastic containers; (b) Setup with a PVC pipe; (c) Fiber wrapped around a cork (15-m long); (d) Fiber wrapped around a coil (15-m long).

2.4. Signal Detection underwater

Subsequently, tests were performed under simulated underwater conditions using two acoustic sources. First, a buzzer CPE-267 was used together with a microphone to compare the reference frequencies emitted with those detected by the optical fiber (Figure

2.13). Then, an EvoLogics 18/34 horizontally omnidirectional acoustic modem was used, traditionally applied for underwater communications, which emitted communication packets between 18 and 34 kHz - Figure 2.14.

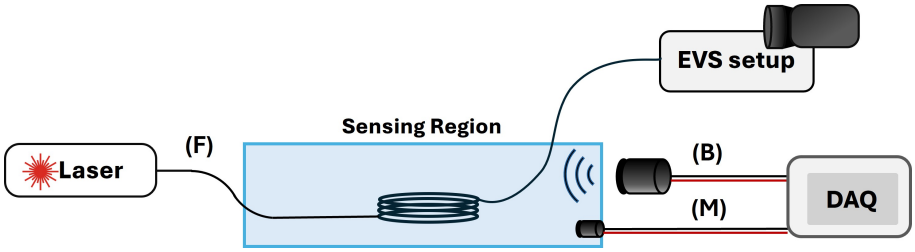

Figure 2.13: Experimental setup: optical fiber in a water tank at low depth. (F) Optical Fiber; (B) Buzzer CPE-267; (M) Omnidirectional microphone CMC-4015-25L100.

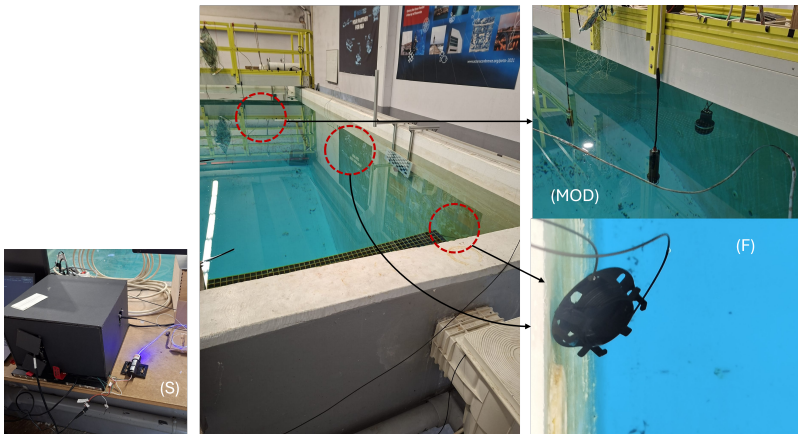

Figure 2.14: Experimental setup: optical fibers in a 5-m depth a water tank with a configuration closer to our end use. (F) Optical Fiber; (MOD) Acoustic Modem; (S) Experimental setup for 2 optical fibers.

Results Firstly, it was possible to detect frequency responses beyond 3 kHz using a piezo buzzer with a resonance frequency of 2.8 kHz and operating voltage between 6 and 14 V, although the DAQ has a maximum operating voltage of 10 V. The maximum SNR obtained with the buzzer was approximately 30 dB for a frequency around 2 kHz (Fig. 2.15). Subsequently, with the acoustic modem located 3 meters from the sensing fiber, sound signals were detected, demonstrating the system capability to operate in representative environmental conditions (Fig. 2.16).

2.4.1 Limitations of Interrogation with EVS

The accumulation time is defined as the time window used over which events are accumulated to retrieve 2D images. This factor needs to be equal or higher than the sensor latency; otherwise, some event information may be lost and some lines can be faded, as

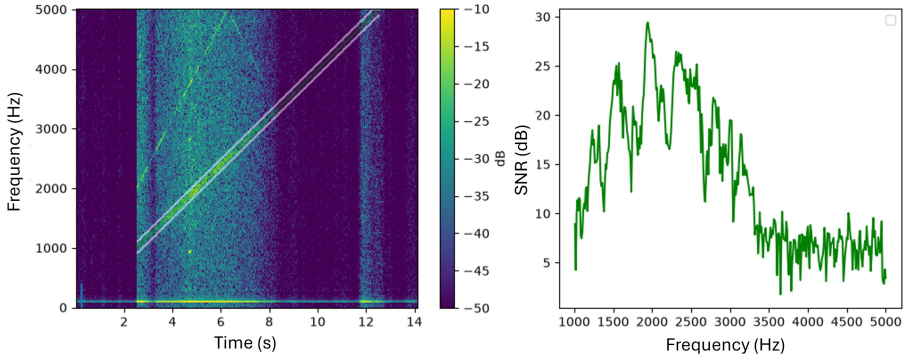

Figure 2.15: (Right) Spectrogram of the signal in response to the chirp emitted by a buzzer underwater. (Left) SNR related to the signal, with a maximum peak of 30 dB.

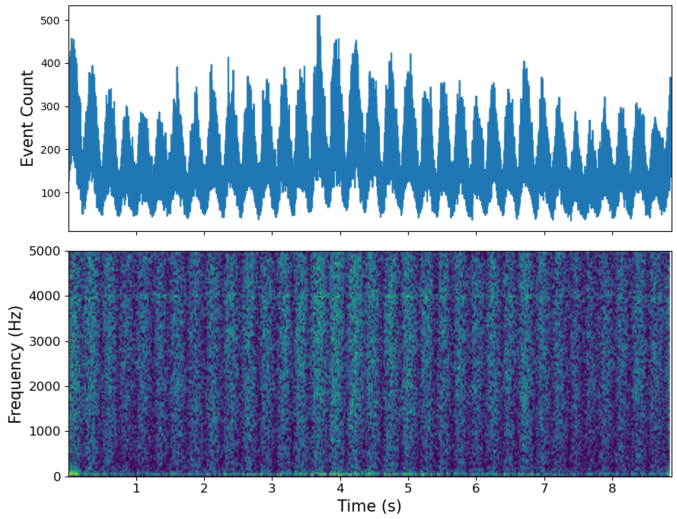

Figure 2.16: Experimental results: (Top) Event count showing the pattern of the bit sequences transmitted by the router; (Bottom) The corresponding spectrogram.

visible in Figure 2.17. The latency increases with the event rate, reaching a maximum value of 450 μs approximately for an event rate of 400 events/μs. Since the readout of events is row-wise, the latency also varies row-wise which justifies the appearance of horizontal artifacts in the reconstructed images [65].

The vertical components, often visible in the spectrograms, are due to constant mechanical perturbations in the water, which happen to have more impact than the acoustic signals emitted.

Other parameters were investigated to determine the reasons behind an inefficient response. These included the laser wavelength and corresponding number of modes propagating in the optical fiber (Fig. 2.18), the size of the predefined ROIs and subsequent number of events activated, and the background illumination conditions. For instance, a blue laser, according to the V-number equation, supports more propagating modes, since

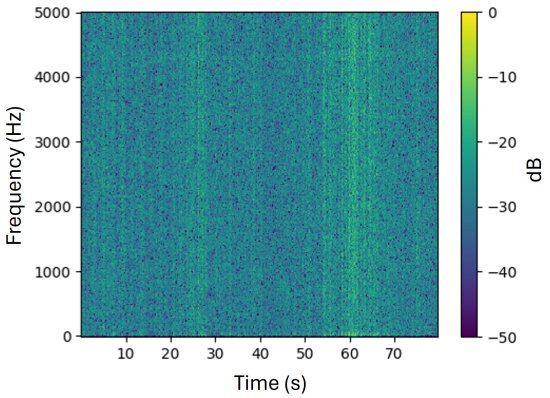

Figure 2.17: Signal obtained due to latency limitations.

it has a wavelength lower than the red one. However, the contrast between ON and OFF events is also lower, which may lead to less generated events, or they need to be more intense to be detected.

Ambient lighting was also found to be important: a dark background results in higher noise levels, whereas a light background requires a greater intensity variation to trigger an event. Therefore, a mean term when it comes to background lighting is necessary, bearing in mind that when the optical beam is already spatially spread, it contributes as background illumination, eliminating the need for additional external light. The size of the selected ROIs was found to be relevant on the measured delays: larger or uneven ROIs can introduce additional latency in the order of milliseconds, as explained before. Furthermore, latency was observed even within a single ROI when its size was sufficiently large. A RGB camera can be used to monitor the intensity of each ROI individually, which is adjusted using linear polarizers and attenuators, as mentioned in Section 2.2, demonstrating their importance to help minimize the imbalance between ROIs.

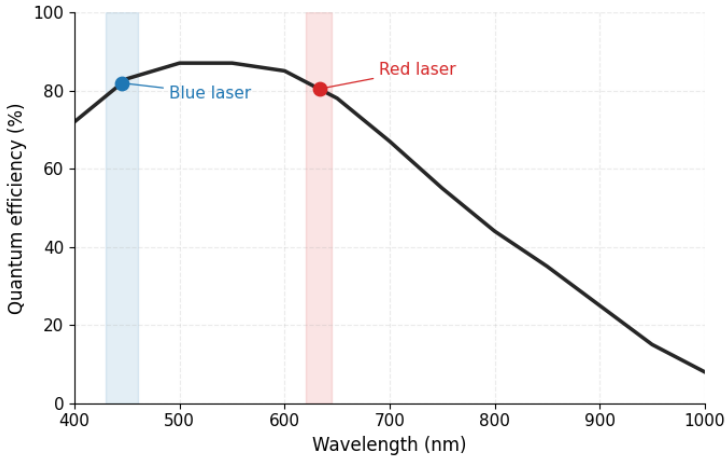

Figure 2.18: Quantum efficiency as a function of wavelength: both lasers blue and red show equal efficiency.

2.5. Sound Localization in two dimensions

With the sound detection system set up in this way, preliminary studies on the location of the acoustic source were also conducted using three optical fibers, allowing for unambiguous 2D location. Using only two fibers, the measured time delay between them defines a hyperbola corresponding to all possible source locations that correspond to the same difference in distance between the source and each fiber. With a third fiber included in the setup, as shown in the figure 2.20, the additional delay information allows the source position to be uniquely determined from the intersection of hyperbolas.

The overall steps for data processing and source position estimation presented in this chapter are summarize in Fig. 2.19.

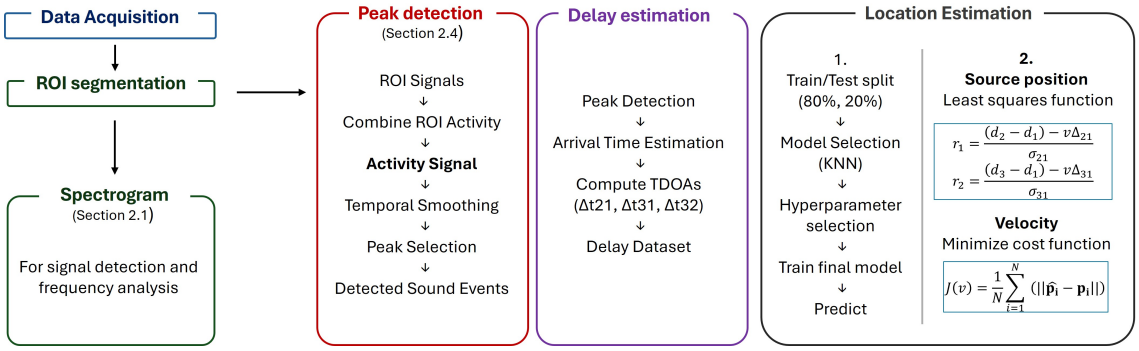

Figure 2.19: Following data acquisition and ROI segmentation, which were discussed previously, the subsequent processing relies on peak detection to determine the signal onset timestamps, critical for our next objective.

2.5.1 Localization using KNN Regression Model

The system was evaluated for surface-based localization, in which time-delay features derived from the event camera are mapped to acoustic impact positions through a K-Nearest Neighbors (KNN) regression model.

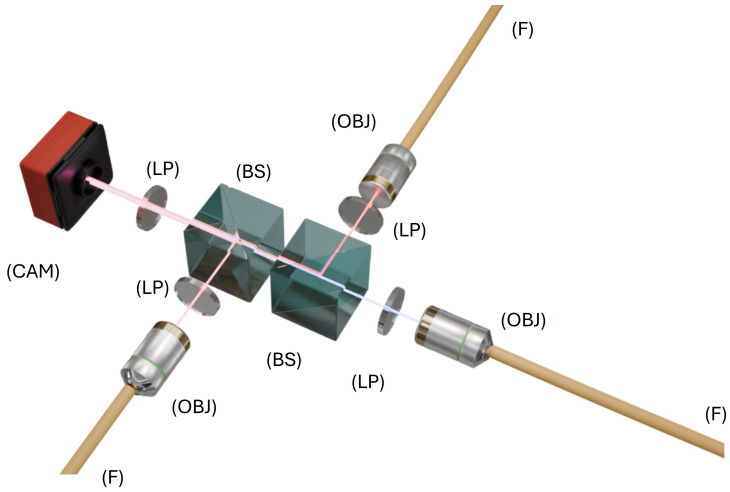

Figure 2.20: Setup with the three fibers for localization. (CAM) EVS; (OBJ) Objective; (O) Optical Fiber; (BS) Beam Splitter; (LP) Linear Polarizer.

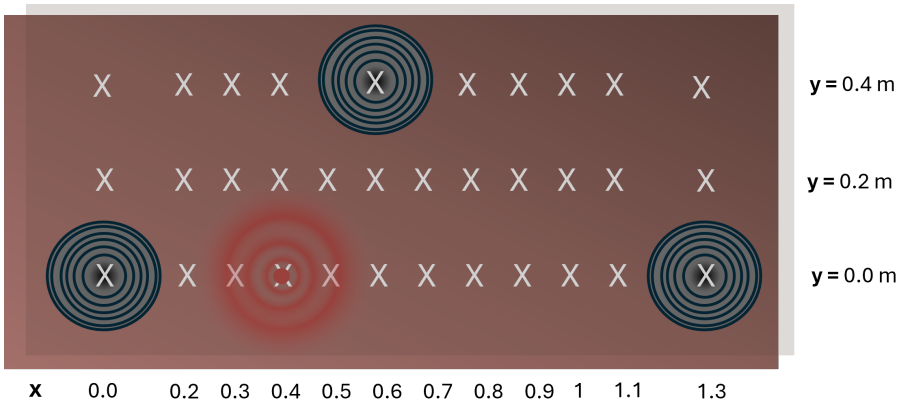

Figure 2.21: Scheme related to experimental tests to locate the sound impacts created in a table.

For this, the three delay measurements were used as input features, computed by:

$$d_{ij} = t_j - t_i, \qquad 1 \leq i < j \leq 3 \tag{2.6}$$

where t_1, t_2, and t_3 correspond to the detected arrival times at each fiber. On the other hand, X and Y contain the target outputs (*x_source* and *y_source*). With that, the model learns the relation:

$$(d_{12},\ d_{23},\ d_{13}) \rightarrow (x_{source},\ y_{source})$$

allowing us to estimate the source position.

The dataset, created from multiple impacts at the 34 different positions represented in the table (Fig. 2.21), is then divided into 80 % for training and 20 % for testing, using a grouped random split. For each K-value tested, the Euclidean localization error between the predicted and true source coordinates was calculated by:

$$\text{error} = \sqrt{(x_{\text{pred}} - x_{\text{true}})^2 + (y_{\text{pred}} - y_{\text{true}})^2} \tag{2.7}$$

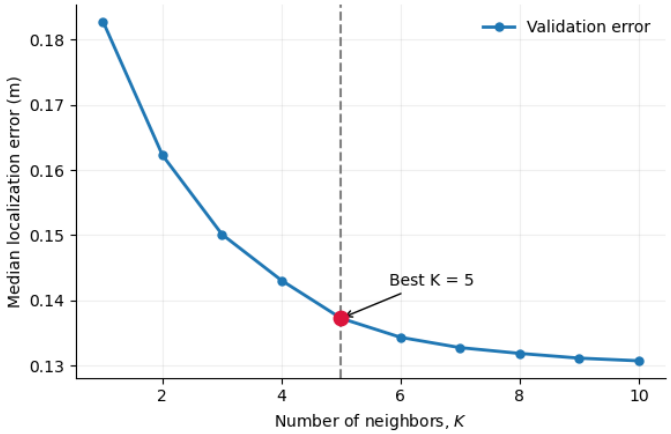

Figure 2.22: Method to choose the K-value based on the ”elbow” criterion, which suggests that additional number of neighbors beyond the selected value may lead to overfitting.

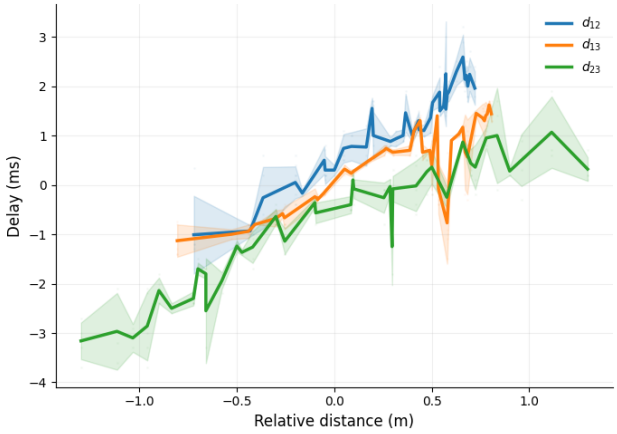

Figure 2.23: Dispersion between the three delays for each position studied.

The results obtained from the validation dataset comprising five random positions are represented in Figure 2.24 and are evaluated based on three metrics: mean, median (less sensitive to outliers) and maximum position error.

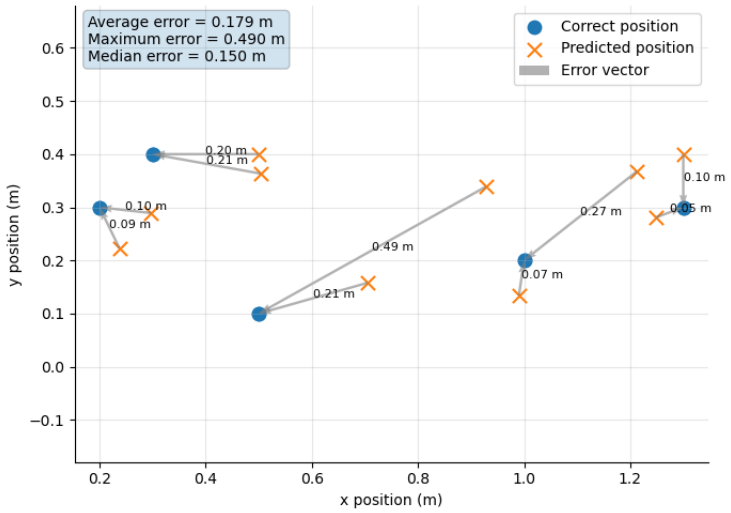

Figure 2.24: Acoustic source localization using the validation dataset, with a maximum error of 49 cm and mean error of 17.9 cm.

2.5.2 Localization using a Physics-based localization Model

To estimate the acoustic source position, another method was found, based on Time Difference of Arrival (TDOA), which turned out to be more robust than using the KNN regression model. Let the unknown impact position be $\mathbf{p} = (x, y)$ and the fibers in known positions $\mathbf{s_1}$, $\mathbf{s_2}$, $\mathbf{s_3}$, such that the Euclidean distance between the fibers and the source impact positions is: $d_i = ||\mathbf{p} - \mathbf{s_i}||$. Hereupon, we got 2 TDOA equations that describe 2 hyperbolas, whose intersection corresponds to the source position (as represented in the left of Figure 2.25):

$$d_2 - d_1 = v\Delta t_{21} \tag{2.8}$$

$$d_3 - d_1 = v\Delta t_{31} \tag{2.9}$$

Δt_{12} and Δt_{31} represent the obtained difference of delays from the fibers and the source.

The source position is estimated by minimizing the residuals using the *least_square* function:

$$r_1 = \frac{(d_2 - d_1) - v\Delta t_{21}}{\sigma_{21}} \tag{2.10}$$

$$r_2 = \frac{(d_3 - d_1) - v\Delta t_{31}}{\sigma_{31}} \tag{2.11}$$

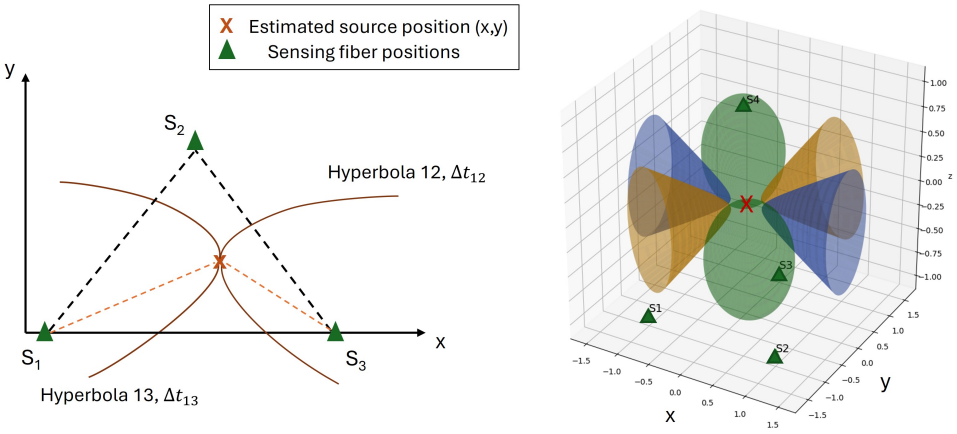

Figure 2.25: Localization solutions according to the fiber configuration: (Left) Source localization using 3 coplanar optical fibers: the measured delays define 2 hyperbolas whose intersection gives the estimated source position in a plane; (Right) Extension to 3D localization using 4 non-coplanar optical fibers (future work).

The mean localization error is then computed:

$$J(v) = \frac{1}{N}\sum_{i=1}^{N}\left(||\hat{\mathbf{p}}_\mathbf{i} - \mathbf{p}_\mathbf{i}||\right) \tag{2.12}$$

And the best velocity value is the one that minimizes the cost function in equation 2.12. In this case, the estimated value was 485 m/s, which is less than the expected velocity in wood (between 1000 and 4900 m/s). This discrepancy can be justified by a combination of factors, namely the background illumination, event camera response, and also uncertainties in the delay estimations.

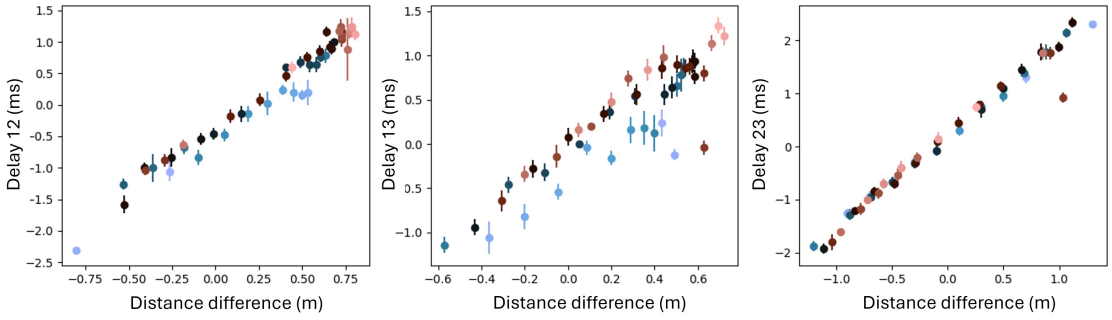

Figure 2.26: Dispersion between the delays and distance differences: although the calculated velocity is not physically meaningful, there is a clear correlation between the delays and the distance differences.

Regarding outlier detection, Figure 2.26 represents the dispersion between the delays obtained and the distance differences after applying a filter that replaces the outlier values *y* by the local median of the remaining values. The Robust Z-score was the technique

selected as it is independent of the ordering of the samples, while Hampel Filter uses a sliding window applied to sequential data.

The results obtained using this model (Figure 2.27) show a mean localization error of 15 cm over the same 1.3 by 0.4 m^2 area; however, the maximum error was 45 cm, which confirms the existence of some outliers possibly due to material heterogeneities in the table that may have led to variations in the propagation velocity of sound waves.

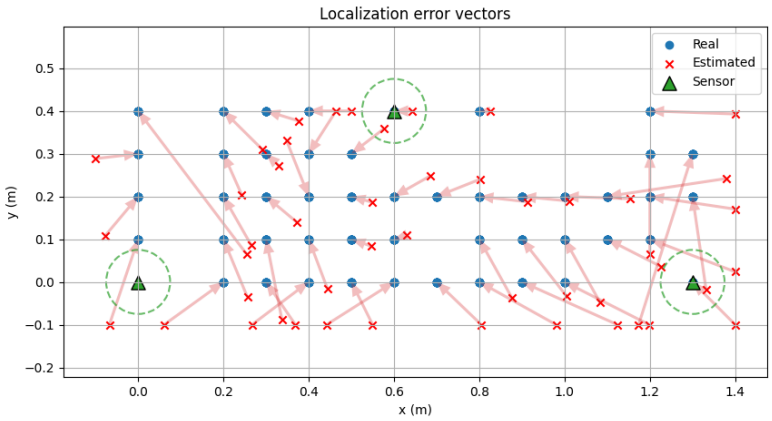

Figure 2.27: Physics-based model results yielding a mean error of 15 cm.

To help improve the performance of peak detection, explained below, the ROIs of the fibers were defined as small areas with horizontal alignment on the sensor, with the help of pinholes, which behave as spatial filters. This configuration minimizes latency, discussed in the previous section, reducing artificial temporal delays and contributing to a more robust method.

2.5.3 Signal Automatic detection

In the initial tests, the delays used for source localization were estimated based on the detection of the signal onset relative to the fiber response, using the function *"detect_peak_starts"* which outlines the following steps:

1. It analyzes the derivative of the filtered signal and, by identifying where it exceeds a chosen threshold, it allows us to determine the onset of a peak caused by an external perturbation;

2. To help filter out noise and ensure that only valid changes are detected, the algorithm requires a certain number of consecutive samples to satisfy that condition;

3. The code then groups nearby detected peaks into clusters, separated by a distance less than a specified maximum gap;

4. Therefore, each cluster represents a single impact event and the timestamp of the first event detected in that cluster is defined as the start of the impact (Figure 2.28 - left).

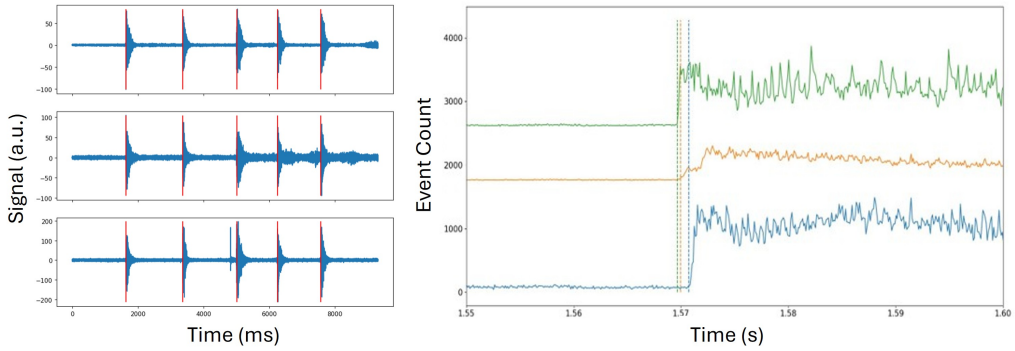

Figure 2.28: Timestamp of the signal start in the three fibers. (Left) Signal onset detection using the derivative, individually; (Right) Events are initially identified when summing the intensity from the three fibers. Once the event window is detected, the onset of the signal for each fiber is estimated.

The onset of the response can also be determined in a more robust way by using a step-event detector that combines two complementary measures: a Haar wavelet-based detector, which identifies sudden changes in intensity, and a normalized sliding correlation, which evaluates the similarity between the measured signal and a given template, by slicing it along the measured signal. This method reduces false detections due to noise, with the earliest significant peak in this score chosen as the arrival time of the acoustic wave at each fiber. Finally, the delays are obtained by subtracting the estimated arrival times between the three fibers.

2.6. Concluding Remarks

In this chapter, the event-based camera and its operating principle were introduced, after enumerating the traditional sensors used for fiber specklegram sensors, their applications, and their limitations. The results obtained in air and underwater were discussed, as well as the difficulties and limitations of the proposed approach. Acoustic signals emitted by an acoustic modem were successfully detected in a water tank, at distances up to 3 meters, while in another configuration, in a low depth tank, frequencies beyond 3 kHz were detected with a SNR maximum of 30 dB.

Besides the characterization of the frequency response based on SNR, it was evaluated the capacity of localize acoustic signals in a two-dimensional plane. For that a set of steps for data acquisition and processing was performed, starting with event streaming and storage, ROI segmentation and then temporal integration, which are crucial to detect the external acoustic signals and evaluate the fiber response. Next, the first peak of each signal is automatically detected in order to compute the delays between the three fibers, necessary for localization. Two methods were performed for that purpose: a KNN regression model, and a physic-based model where the position was estimated through the least squares function to minimize the cost function. The second method yielded results of a mean error of 15 cm, within an area of test of 1.3 by 0.4 m^2, comparable to the best results obtained with the first technique; however, it proved to be more robust and consistent.

3. State of Polarization Interrogation for Acoustic Signal Classification and Reconstruction

Light is an electromagnetic wave characterized by oscillating electric and magnetic fields that propagate together in the same direction and at the same velocity. For a plane electromagnetic wave, the electric and magnetic fields are mutually orthogonal and both perpendicular to the direction of propagation. The polarization of light describes the orientation and temporal evolution of the electric field, $\vec{E}$, in the plane perpendicular to the direction of propagation. The electric field can, in turn, be decomposed into two orthogonal components:

$$\vec{E} = E_x(z,t) + E_y(z,t) = E_{0x}(t)e^{i(\omega t - kz + \delta_x(t))} + E_{0y}(t)e^{i(\omega t - kz + \delta_y(t))} \tag{3.1}$$

The polarization state can be quantitatively described using the Stokes parameters, introduced by George Gabriel Stokes in 1851 [66]. The polarization state of the light propagating in the fiber can be represented as:

$$\vec{S} = \begin{pmatrix} S_0 \\ S_1 \\ S_2 \\ S_3 \end{pmatrix} = \begin{pmatrix} E_{0x}^2 + E_{0y}^2 \\ E_{0x}^2 - E_{0y}^2 \\ 2E_{0x}E_{0y}\cos\Delta\delta \\ 2E_{0x}E_{0y}\sin\Delta\delta \end{pmatrix} \tag{3.2}$$

where $\Delta\delta = \delta y - \delta x$ represents the phase difference between the two orthogonal components of the electric field.

The parameter S_0 represents the total optical intensity, while S_1 describes the intensity difference between horizontally and vertically polarized components; S_2 represents the intensity difference between linear polarization components oriented at $+45^\circ$ and -45°, and the parameter S_3 describes the difference between the two circular polarization components, with the sign depending on the adopted handedness convention. The Stokes parameters satisfy the relation:

$$S_0^2 \geq S_1^2 + S_2^2 + S_3^2 \tag{3.3}$$

where the equality holds for completely polarized light.

The polarization state of light can be represented geometrically using the Poincaré sphere, introduced by Henri Poincaré in 1892 [67] as can be seen in Figure 3.1. The sphere is defined by the normalized Stokes parameters $(s_i = S_i/S_0)$, with $(i = 1,2,3)$. Fully polarized states lie on the surface of the sphere, with different points corresponding to linear, circular, or elliptical polarization states.

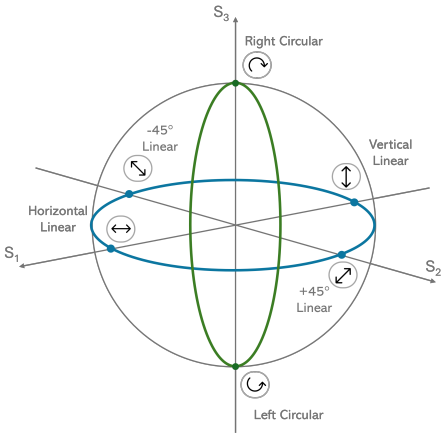

Figure 3.1: Polarization states mapped in the Poincaré sphere.

In addition to describe the polarization state, the Stokes parameters also quantify the degree to which light is polarized through the Degree of Polarization (DOP), defined as

$$DOP = \frac{\sqrt{S_1^2 + S_2^2 + S_3^2}}{S_0} \tag{3.4}$$

A DOP of 1 corresponds to fully polarized light, while lower values indicate partial polarization. While the DOP describes the extent to which the optical field is polarized, the State of Polarization (SoP) can also evolve as light propagates through an optical medium. In particular, when a medium exhibits birefringence, the two orthogonal polarization components experience different refractive indices and therefore accumulate a relative phase delay during propagation. This phase difference modifies the SoP, which can be visualized as a trajectory in the Poincaré sphere.

Birefringence is an optical property of anisotropic media in which two orthogonal polarization components propagate with different effective refractive indices. These components define the fast and slow optical axes of the medium, with corresponding refractive indices n_f and n_s. The birefringence can be defined as $B = n_s - n_f$. As the two components propagate, the difference in their propagation constants results in the accumulation of a relative phase difference:

$$\Delta\phi = \frac{2\pi}{\lambda}\Delta n L, \tag{3.5}$$

where Δn is the birefringence, L is the fiber length, and λ is the optical wavelength.

As the relative phase difference evolves, the SoP varies periodically along the propagation direction. The distance required for the phase difference to reach 2π is known as the beat length, L_b, and can be expressed as

$$L_b = \frac{\lambda}{|\Delta n|}. \tag{3.6}$$

In optical fibers, birefringence arises from breaking the transverse symmetry, which may result from geometrical asymmetries, such as core ellipticity, residual stress induced during fabrication, or externally applied perturbations such as stress, bending, or twisting as described in Figure 3.2. As a result, an arbitrary input polarization state can be decomposed into two orthogonal polarization modes, which propagate along the fiber with different effective refractive indices.

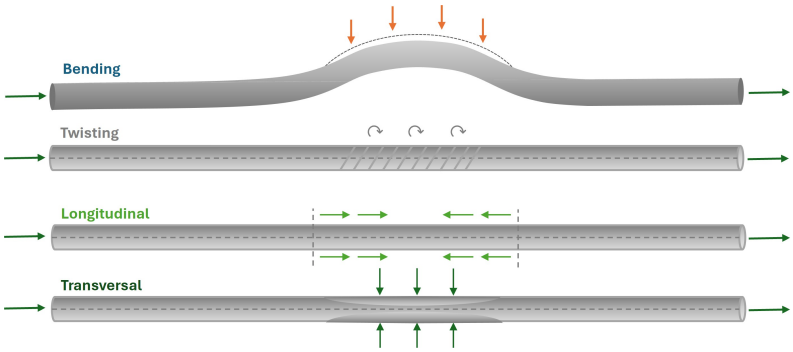

Figure 3.2: Types of deformations applied on the fiber: bending, which creates linear birefringence; twisting, that changes the refractive index profile non-uniformly over its cross-section; longitudinal deformation and even transversal caused by flattening the fiber, but not as effective as the first two, which break the symmetry of the fiber.

Extrinsic perturbations applied in the optical fiber, such as strain, vibration and acoustic waves, can modify its birefringence and induce coupling between polarization modes, altering the SoP which leads to measurable temporal variations in the output polarization state. Polarization-based sensors exploit these variations to infer information about the perturbations acting on the fiber.

The sensitivity to environmental perturbations, combined with the possibility of interrogating optical fibers over long distances, has motivated the use of polarization-based

measurements for large-scale monitoring. Recent studies have explored their application to strain, temperature, and vibration sensing, as well as to the detection of climatic and geophysical phenomena such as earthquakes and tsunamis [68, 69].

Beyond the work of Orlando Galicio *et al.* [33], discussed in the previous chapter, which explored the detection of geophysical events with electronic systems based on multimode fiber speckle patterns, polarization-based approaches have also been explored using existing telecommunication infrastructure. Zhan *et al.* demonstrated that submarine telecommunication cables can be used to detect seismic and ocean waves over distances exceeding 10.000 km [70]. In 2021, building on this concept, Costa *et al.* [37] not only detected seismic events, but also successfully localized the epicenter of the 2022 Guerrero (Mexico) earthquake with magnitude $M_w = 6.0$ using an existing transoceanic cable between Los Angeles and Valparaíso, demonstrating scalable and infrastructure-compatible offshore seismic monitoring.

Beyond distributed sensing (Figure 3.3), polarization-based techniques have also been widely explored for point-sensing applications. By monitoring changes in the polarization state or polarization-dependent response of an optical system, a range of physical and chemical parameters can be measured with high sensitivity. For example, combining polarization-sensitive interrogation techniques with FBGs enables the measurement of temperature, pressure, and axial strain, with applications extending to biochemical sensing [71]. Polarization-based sensing has also had an impact on chemical sensing, for example, with hydrogen sensors based on polarization-diversity loop interferometers consisting of a Polarization Beam Splitter (PBS), two quarter-wave plates and a polarization-maintaining (PM) fiber [72].

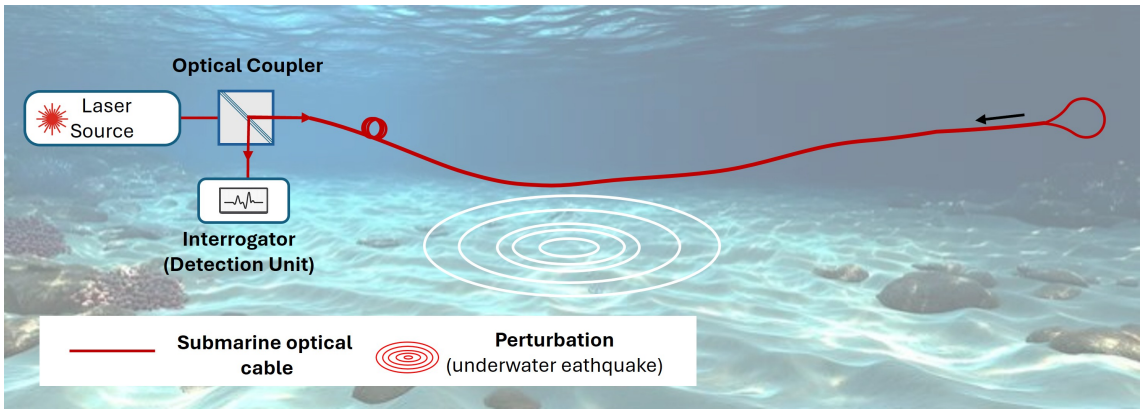

Figure 3.3: Polarization-based sensing for geology studies, namely for seismic monitoring.

This chapter first presents the experimental setup and characterization of the polarization-based sensing system using a commercial polarimeter, followed by its application to acoustic signal classification. The chapter then explores two alternative interrogation configurations developed to reduce the cost and complexity of the system and improve its suitability for integration into robotic platforms.

3.1. Experimental Characterization of Polarization-Based Acoustic Sensing

To evaluate polarization-based acoustic sensing experimentally, the response of optical fibers to controlled acoustic perturbations was investigated under different conditions. Measurements were performed in both air and water, using different fiber configurations to assess the influence of the surrounding medium and fiber arrangement on the polarization response. The resulting variations in the output state of polarization were monitored using a commercial polarimeter. A schematic diagram of the experimental setup is shown in Figure 3.4. The optical interrogation was performed using a tunable laser (Thorlabs TL200C) set to a wavelength of 1550 nm, while output state of polarization was monitored using a commercial high-speed polarimeter (Novoptel PM1000). The polarimeter supports acquisition rates of up to 100 MSamples/s, corresponding to a maximum theoretical measurement bandwidth of 50 MHz according to the Nyquist criterion. The experiments were performed using an approximately 4-m-long single-mode fiber, with the sensing region arranged in different geometrical configurations to evaluate their influence on the sensitivity to acoustic perturbations.



Figure 3.4: Experimental setup for polarization-based acoustic sensing. Light from a 1550 nm laser is coupled into the single mode fiber serving as the sensing fiber with a sensing region with different geometric configurations, and the output state of polarization is measured using a high-speed polarimeter.

The polarization-based sensing system was experimentally characterized under both airborne and underwater conditions. A piezoelectric actuator was driven with frequency chirps covering the range of interest, while the corresponding variations in the output state of polarization were continuously recorded with the polarimeter. The measurements showed a response up to approximately 12 kHz in air, while a reduced bandwidth of approximately 8 kHz was observed underwater. This difference indicates that the interaction

between the acoustic field and the sensing fiber is strongly influenced by the surrounding medium and by the mechanical conditions under which the fiber is deployed.

In addition to the surrounding medium, the influence of the sensing-fiber geometry was investigated by testing different arrangements, including linear, coiled, and S-shaped configurations. Figures 3.5a and 3.5b compare representative underwater measurements obtained with the fiber in linear and coiled configurations, respectively. In both cases, a frequency chirp was applied and the corresponding polarization response was analyzed in the frequency domain. For the linear configuration, the applied frequency components were clearly recovered over the investigated range, with a mean SNR of 23.71 dB, as shown in Figure 3.5a. When the fiber was arranged in a coil, the mean SNR decreased to 14.02 dB (Figure 3.5b). Similar behavior was observed for different numbers of loops, indicating that increasing the number of turns did not improve the acoustic sensitivity under the tested conditions. The S-shaped configuration also showed no improvement relative to the linear arrangement.

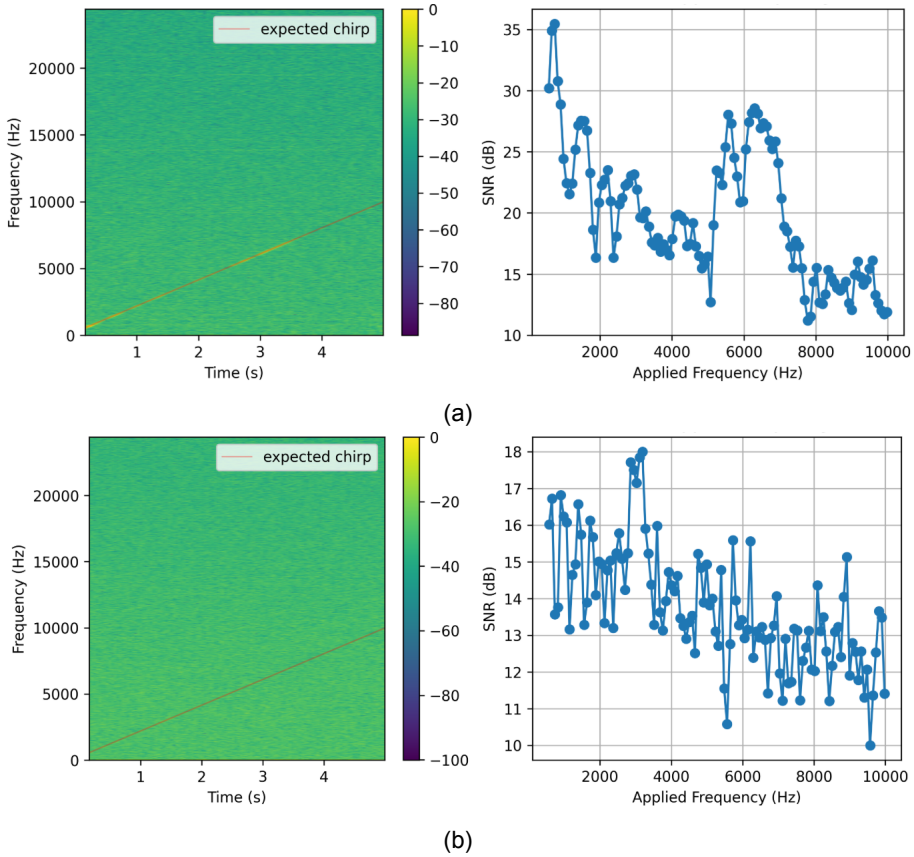

Figure 3.5: Frequency response to a chirp up to 10 kHz with the sensing fiber submerged in water: (a) linear configuration and (b) coiled configuration. The left panels show the spectrograms of the measured SoP variations, with the line indicating the excitation frequency of the piezoelectric actuator, while the right panels show the corresponding SNR as a function of the applied frequency.

These results suggest that, under the present experimental conditions, maintaining the sensing region in a straight configuration provides more efficient coupling between the acoustic perturbation and the polarization response of the fiber.

3.2. Sound Source Classification

Beyond acoustic perturbation detection, polarization measurements can also be used for classification of objects, by establishing a relation between the variations of the SoP and the mechanical deformation applied to the optical fiber. To establish the relationship between the applied perturbation and the resulting polarization changes, an initial calibration is performed using a sinusoidal excitation of known amplitude and frequency applied to the fiber through a piezoelectric actuator. The polarization response is represented by the normalized Stokes vector, $\mathbf{S} = [S_1, S_2, S_3]$.

During calibration, the polarization state measured in the absence of an applied perturbation defines the reference state, $\mathbf{S}_{\text{ref}}$. The perturbed state, $\mathbf{S_{stim}}$, is obtained from the normalized Stokes parameters measured when the sinusoidal excitation reaches its maximum amplitude. The change in polarization between these two states therefore represents the response of the fiber to a known perturbation and is used to determine the sensitivity vector, $\mathbf{m}$, which relates variations in the measured SoP to the amplitude of the applied stimulus. Once the sensitivity vector has been determined, the temporal waveform can be reconstructed from the measured polarization variations, $\mathbf{S(t)}$, according to

$$x(t) = [\mathbf{S(t)} - \mathbf{S_{ref}}]\ \mathbf{m} \tag{3.7}$$

The reconstruction signals were used as input for classification. For each recording, Mel-Frequency cepstral coefficients (MFCCs) were extracted to characterize the spectral properties of the reconstructed waveforms. Aside from the MFCCs, additional features related to the mean and standard-deviation of the signal and the power spectral density were extracted. The combined feature set provided improved discrimination between the two signal classes compared with the use of MFCCs alone. However, the inclusion of amplitude- and power-related features may make the classification more sensitive to variations in excitation intensity. The resulting feature vectors were used to train a KNN classifier to distinguish between the two classes, denoted as ”Type 1” and ”Type 2”. Once trained, the same processing pipeline can be applied to incoming polarization measurements: the perturbation waveform is reconstructed using the previously determined sensitivity vector,

its features are extracted, and the trained classifier assigns the measurement to one of the two classes. This enables the polarization-based sensing system to provide not only information on the applied perturbation but also real-time identification of the corresponding signal class.

The complete reconstruction and classification pipeline is summarized in Figure 3.6. The procedure was evaluated using four independent datasets, each containing 20 recordings and obtained using a separate calibration measurement. Across these datasets, a mean classification accuracy of 85% was achieved.

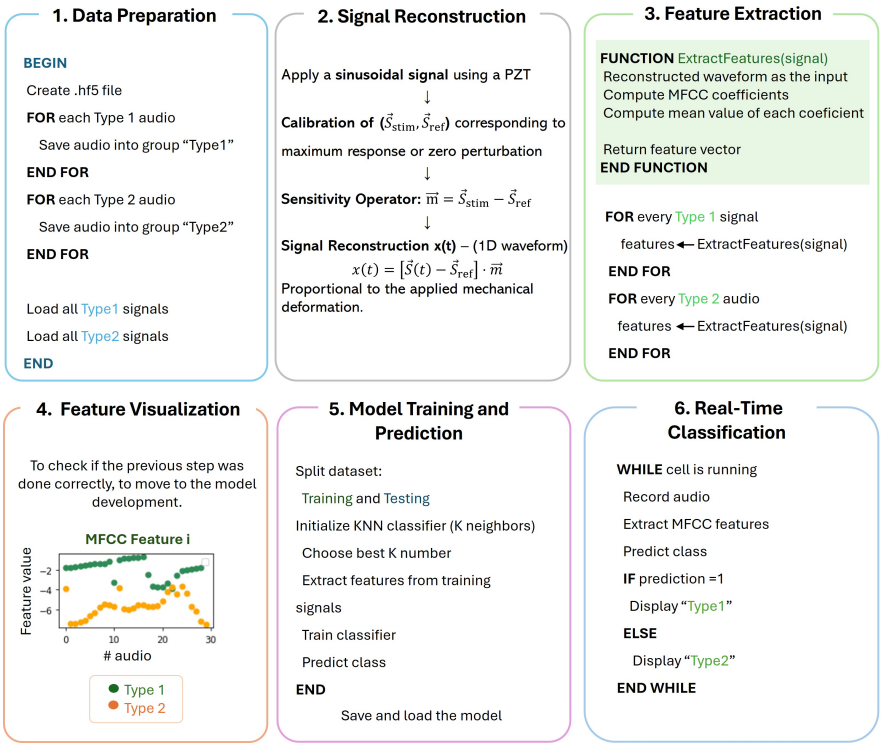

Figure 3.6: Acquisition data and processing for objects classification procedure.

3.3. Towards low SWaP-C polarimeter setups

While the commercial polarimeter provides high-speed and complete characterization of the SoP, its size, cost, and complexity make it less suitable for integration into an AUV or ROV. Therefore, simplified interrogation schemes were investigated with the aim of reducing the size, weight, power consumption, and cost (SWaP-C) of the sensing system while retaining sensitivity to perturbation-induced polarization changes.

One of the studied configurations, represented in Figure 3.7, replaces the commercial polarimeter with a reduced set of fiber-based optical components and photodetectors.

Light from a 1550 nm laser (Thorlabs TL200C) is coupled to a single mode fiber traveling into the sensing region. The output is coupled into a 70:30 fiber coupler that splits the light evenly into two optical paths: one is used to monitor the total optical intensity, corresponding to S_0, while the other is directed to a polarization splitter, which separates the optical signal into two orthogonal polarization components, I_V and I_H. Changes in the polarization state therefore produce variations in the relative optical intensities measured at the two outputs. Due to restrictions, only 2 outputs were measured, the reference path and one of the outputs of the polarization splitter using 2 InGaAs photodetectors (Thorlabs DET01CFC). As this experimental setup does not allow to assess the full SoP, a polarization controller was used to optimize the output signal. This interrogation system was evaluated under different experimental conditions to determine whether it provided sufficient sensitivity for acoustic sensing. Initially, the SMF was directly coupled to a piezoelectric actuator to maximize the mechanical interaction between the applied perturbation and the fiber. However, the resulting variations in the measured polarization components were insufficient for reliable signal detection. The experiments were then extended to an underwater configuration, where different fiber geometries were investigated to modify the interaction between the acoustic field and the sensing fiber and potentially enhance its response. Despite these changes, no clear improvement in the detected signal was observed, indicating that the sensitivity of the simplified interrogation scheme remained insufficient under the tested conditions.

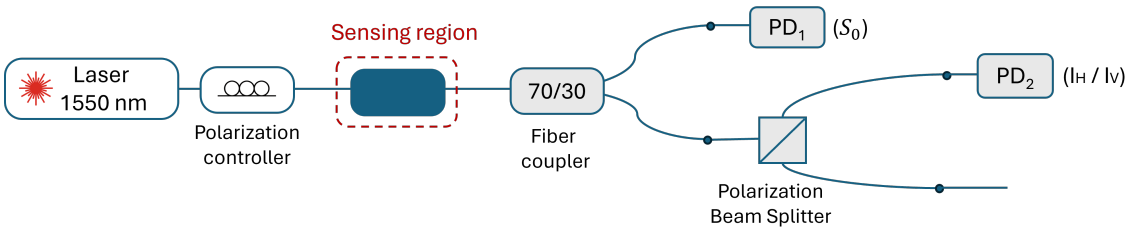

Figure 3.7: Experimental setup for the simplified interrogation scheme, using a polarization splitter to monitor orthogonal polarization components.

Since the first approach monitors only a limited projection of the polarization state, a second interrogation scheme was investigated to recover all three normalized Stokes parameters. This provides access to the complete SoP evolution and is expected to improve sensitivity to perturbation-induced polarization changes while maintaining a compact, low-SWaP-C architecture. The second experimental approach, shown in Fig. 3.8, consists on a fiber-coupled collimator to collimate the light, subsequently divided into four measurement paths. Three channels use linear polarizers oriented at different angles to provide

the intensity projections required to determine the linear Stokes components. The fourth channel incorporates a quarter-wave plate $(\lambda/4)$ followed by a linear polarizer, providing the additional polarization projection required to determine the circular Stokes component, S_3. The four intensity measurements can therefore be combined to reconstruct the full-Stokes vector $[S_0, S_1, S_2, S_3]$. The light of each optical path was acquired with low-cost high-speed InGaAs photodetectors (Marktech MTPD1309SL-030), whose electrical output are acquired and digitized using an ESP32-C6-DevKitC-1 development board.

The polarizers and quarter-wave plate were calibrated prior to the measurements to ensure an accurate reconstruction of the polarization state. Experimental characterization of the complete acquisition system resulted in a maximum simultaneous sampling rate of 4 kHz across the four photodetector channels. Although this configuration enables reconstruction of the complete SoP using a considerably more compact interrogation system, the achieved acquisition rate was insufficient for the acoustic frequency range targeted in this work.

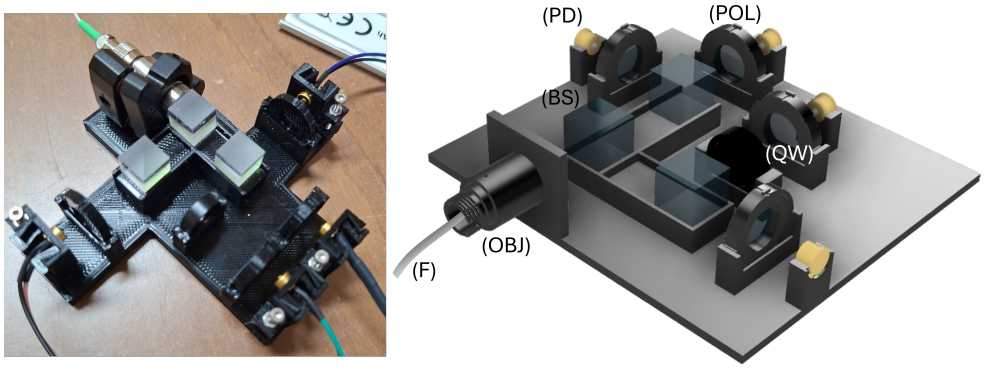

Figure 3.8: Second setup scheme: (POL) polarizer; (OBJ) objective; (PD) photodetector; (BS) beam splitter; (QW) quarter-wave plate; (F) optical fiber.

3.4. Concluding Remarks

This chapter focused on polarization-based sensing for the detection and characterization of acoustic perturbations. The system was first experimentally characterized using a commercial high-speed polarimeter, which enabled the monitoring of perturbation-induced variations in the SoP. Measurements were performed in both air and water, with the underwater experiments considering linear, coiled, and S-shaped fiber configurations. Among the tested geometries, the linear configuration provided the highest sensitivity, in

contrast to the behavior observed for the multimode-fiber sensing approach presented in Chapter 2.

The measurements obtained with the commercial polarimeter were further used to investigate sound classification. Following calibration and waveform reconstruction, features were extracted from the reconstructed signals and used to train a KNN classifier. For two signal classes, a mean classification accuracy of 85 % was obtained across four datasets, each containing 20 recordings and acquired using independent calibration measurements.

Finally, two lower-cost and more compact interrogation configurations were investigated as alternatives to the commercial polarimeter, with the aim of developing a system more suitable for integration into robotic platforms. The first approach, based on a polarization splitter, provided insufficient sensitivity under the tested conditions. The second enabled reconstruction of the complete SoP using four photodetector channels and dedicated acquisition electronics, but its 4 kHz sampling rate limited the accessible acoustic bandwidth. These results identify the main limitations of the current implementations and provide a basis for further optimization of a compact, low-SWaP-C polarization interrogation system.

4. Multimodal System with Event-Based Vision and Polarization Sensing

Multimodal sensing is widely integrated in underwater robotics, where different sensing technologies are combined to exploit their complementary capabilities. Acoustic and optical sensing are often combined, with optical techniques being particularly suited for close-range underwater tasks, while acoustic sensing enables operation over long distances and under conditions of limited visibility [73, 74].

The sensing architecture proposed in this chapter combines the methods presented in Chapters 2 and 3. Polarization interrogation provides high-bandwidth measurement of the perturbation acting on the fiber but, in the configuration considered, does not provide information about its spatial location. In contrast, speckle-based sensing enables to get spatial information about the perturbation but provides limited bandwidth which constrains its ability of reconstruction of high-frequency signals. The two modalities therefore provide complementary information: speckle dynamics can be used for localization, while polarization provide high-bandwidth signal reconstruction capabilities.

To investigate this complementary operation, the speckle-based system, comprising a multimode optical fiber interrogated with an EVS, was operated simultaneously with the polarization-based system, comprising a single-mode optical fiber and a high-speed polarimeter. The data acquisition from both systems was recorded synchronously using parallel threads implemented in Python. The main steps of the acquisition and processing workflow are summarized in Figure 4.1.

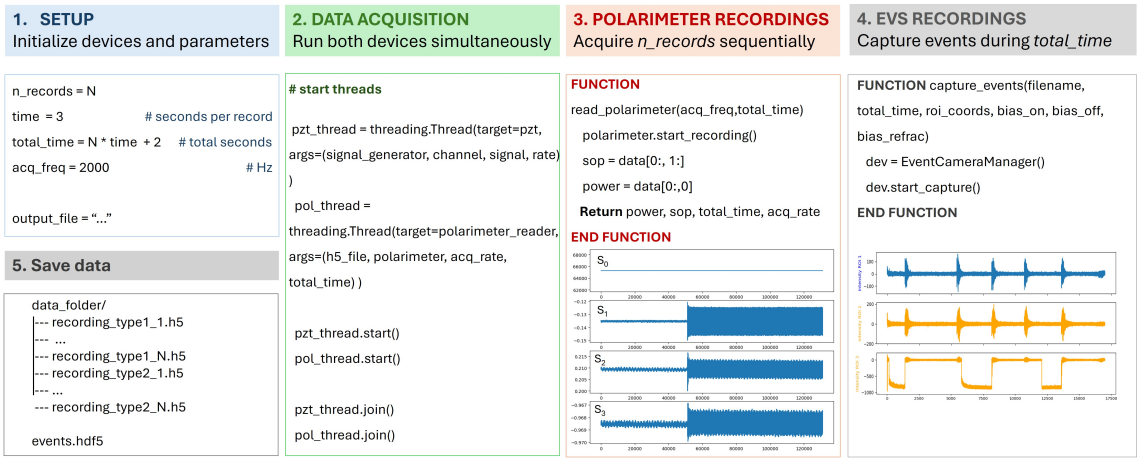

Figure 4.1: Multimodal sensing workflow for simultaneous acquisition and processing of polarimeter and EVS data.

By combining these two modalities, we aim to achieve a real-time sensing system with higher temporal resolution, more informative, and robust than employing either technique alone.

4.1. Experimental results: simultaneous localization and classification

The multimodal sensing approach was tested by combining the two interrogation systems within the same sensing region. Three multimode polymer fibers with a core diameter of 1 mm and a total length of 20 m, denoted as Fiber 1, Fiber 2, and Fiber 3, were positioned at different locations and simultaneously interrogated using the event-based imaging system, providing the spatial information required for perturbation localization. A single mode fiber was placed within the same sensing region and connected to the commercial polarimeter to acquire the corresponding polarization response, allowing simultaneous monitoring through speckle and SoP variations. The complete experimental configuration is shown in Figure 4.2.

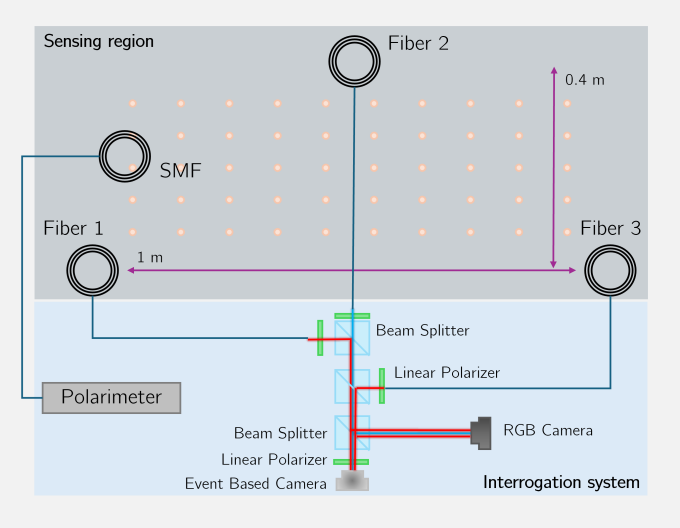

Figure 4.2: Experimental setup for the multimodal sensing approach. Three multimode sensing fibers are distributed across the sensing region and interrogated using the event-based camera, while the single-mode fiber (SMF) is simultaneously monitored using the polarimeter.

To evaluate the feasibility of integrating the two sensing modalities, impact events were created on 43 different positions within the sensing region, following a procedure similar to that described in Chapter 2 and represented as real positions in Figure 4.3b. At each position, we made ten impacts: five with a balldriver and five using a rod, resulting in a total of 430 events. The corresponding speckle and polarization responses were acquired

simultaneously using the EVS and the polarimeter, respectively. The polarization measurements were processed following the reconstruction and feature-extraction procedure described in Chapter 3, with the resulting features used to distinguish between the two types of impact using a KNN classifier.

The classification model was evaluated using a stratified train-test split, preserving the relative proportion of each class in both subsets. To assess the influence of the data partition, the procedure was repeated for 100 different `random_state` values. The resulting accuracies ranged from 90.58 % to 99.28 %, with a mean value of $96.34 \pm 1.66\%$. The variation between splits can be attributed to the relatively limited dataset and to the sensitivity of the KNN algorithm to the distribution of samples in the feature space. Different partitions may therefore result in training sets that represent the variability within each class differently, particularly considering variations in impact position and intensity. Nevertheless, the consistently high accuracy across the different splits indicates that the extracted polarization features provide good discrimination between the two impact classes. The localization performance obtained from the speckle-based measurements is presented in Figure 4.3. For the dataset with 43 impact positions, a mean localization error of 17.8 cm was obtained, with a maximum error of 54.7 cm. For the validation dataset, consisting of eight different positions with two impacts performed for each class at each position, the mean localization error increased slightly to 21.8 cm, while the maximum error decreased to 45.5 cm. Despite the smaller number of positions considered in the validation dataset, the mean errors obtained for both datasets are comparable, indicating a consistent localization performance across the sensing region.

For the validation dataset, the polarization measurements were simultaneously used to classify impact type. The classification results are summarized by the confusion matrix in Figure 4.4, demonstrating the combined capability of the system to provide both spatial information from the speckle response and information about the classification of the type of impact from the polarization response.

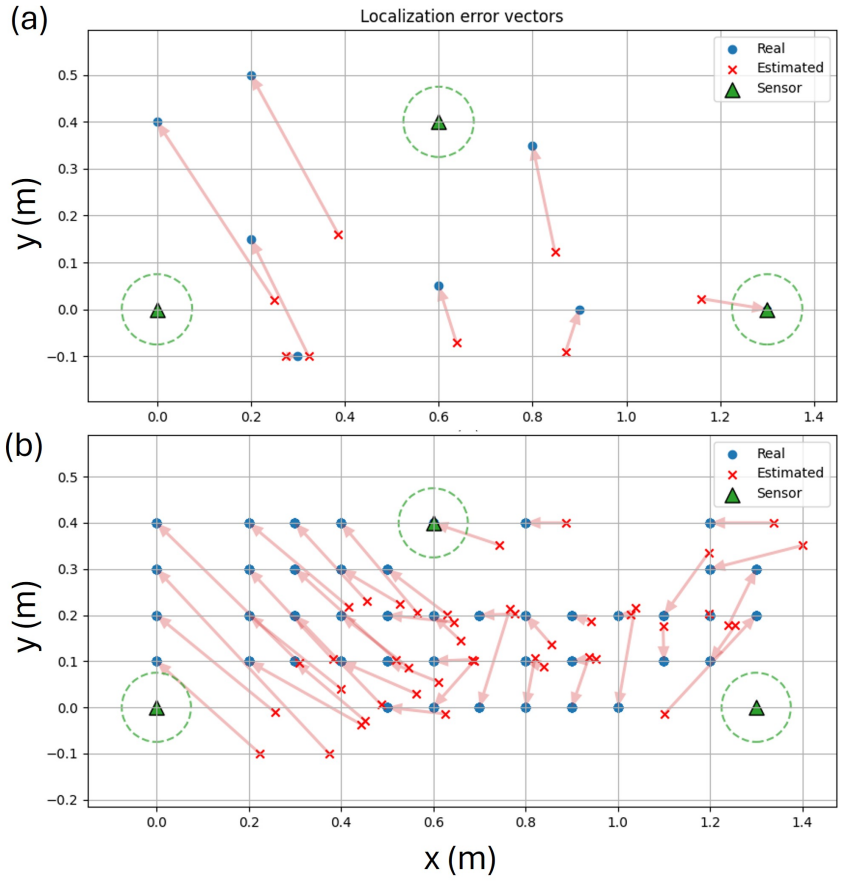

Figure 4.3: Localization error map: (a) using the dataset of 8 points: mean error of 21.8 cm and maximum error of 45.5 cm; (b) using the dataset with 43 points, used for training classification: mean error of 17.8 cm and maximum of 54.7 cm.

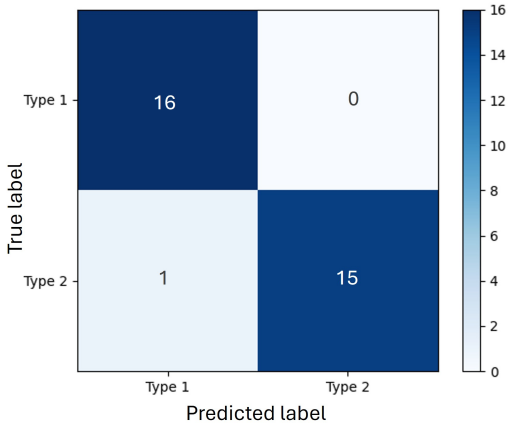

Figure 4.4: Confusion Matrix regarding classification of validation dataset.

4.2. Concluding Remarks

In summary, the proposed multimodal sensing architecture combines the complementary strengths of event-based speckle sensing and polarization interrogation. It was found that

the synchronous acquisition of both modalities established a unified sensing framework that paves the way for a more advanced signal analysis, including event classification, localization, and acoustic signal reconstruction. The results provide a proof of concept for multimodal optical fiber sensing for real-time multipoint monitoring applications. Preliminary results show a mean classification accuracy of approximately 96 % and a mean error of 17.8 cm for a 43-position dataset. Although further experiments are required to assess the performance under more representative conditions, these initial results demonstrate the feasibility of the combined sensing approach.

5. Final Remarks and Future Work

In this work, alternative sensing modalities were presented in order to address some limitations of conventional sensors employed in underwater robotics, particularly in terms of spatial resolution, system complexity, cost, and operation in challenging underwater environments.

The first part of this work focused on speckle-based acoustic sensing using event-based vision sensors. Different optical fibers and sensing configurations were experimentally investigated, and the system response was characterized through spectral and time-frequency analysis. In air, acoustic signals were successfully detected with a SNR on the order of 20 dB. The approach was also validated underwater, where acoustic signals emitted by an acoustic modem were detected at distances of up to 3 meters. In addition to detection, acoustic source localization was also investigated using both KNN regression model and a physics-based model. Maximum errors of 49 cm and 45 cm, respectively, within an area of 0.4 by 1.3 m^2, with the physics-based approach showing greater robustness.

A complementary approach was then investigated, centered on polarization-based sensing. The perturbation-induced variation in the SoP were monitored using a high-speed polarimeter, providing substantially higher acquisition rate, enabling improved reconstruction capabilities of the acoustic waveform. The reconstructed signals were also explored for source classification, achieving a mean accuracy of 85 % for two classes. In parallel, two simplified polarization interrogation architectures were investigated as lower-cost and more compact alternatives to the commercial polarimeter. Although these configurations demonstrated the possibility of reducing system complexity, their current sensitivity and acquisition bandwidth remain insufficient for the targeted application.

Finally, the two sensing modalities were combined into a multimodal system for simultaneous localization and classification. Preliminary experiments demonstrated the feasibility of this combined approach, achieving a mean classification accuracy of approximately 96% and a mean localization error of 17.8 cm for the 43-position dataset. Although further validation is required, these initial results establish a basis for the development of a compact multimodal fiber-optic sensing system for underwater robotic platforms, as conceptually illustrated in Figure 5.1.

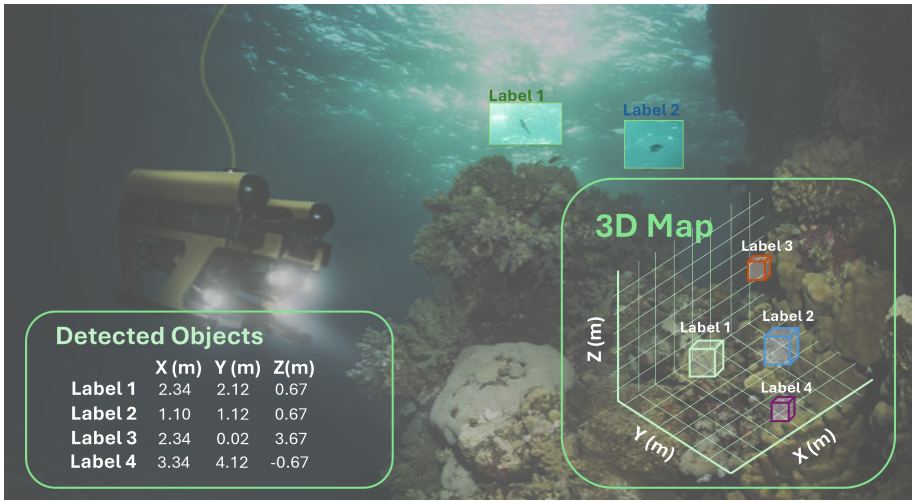

Figure 5.1: Illustration of the capabilities of our final setup regarding 3D location and classification in real underwater environments (Adapted from [75]).

Future work focuses on extending the capabilities demonstrated towards a compact multimodal sensing system suitable for operation in representative underwater environments. One of the main objectives it to extend acoustic source localization from two to three dimensions. This will require an additional spatial sensing channel, together with the adaptation and validation of the localization method to estimate the three spatial coordinates.

The classification approach should also be extended beyond the two classes considered in this work, to be more representative of real environments underwater. For that, it is needed labeled training recording for each class and features that are sufficiently discriminative between all classes. Further underwater experiments are therefore expected using a compact multimodal sensing system easily integrated into autonomous underwater vehicles, with the goal of evaluating its performance under real conditions, including tests to evaluate its omnidirectional capabilities.

Further development of the compact polarization interrogation system is also required. The two alternative configurations investigated in this work provide a starting point for replacing the commercial polarimeter with a lower-SWaP-C solution. Nevertheless, advanced tests are needed to improve their sensitivity and acquisition rate which, in previous tests, was found to be only 4 kHz.

The final objective is to develop a more accurate and robust underwater sensing system, capable of detect and estimate the position of any acoustic source in real environments, as well as distinguish the nature of them, for instance, differentiating boats from animals

or geological/natural events. The integration of this sensing system into an AUV system should also be investigated, with particular attention to minimize its space requirement while being completely functional and ensuring omnidirectional detection capability.

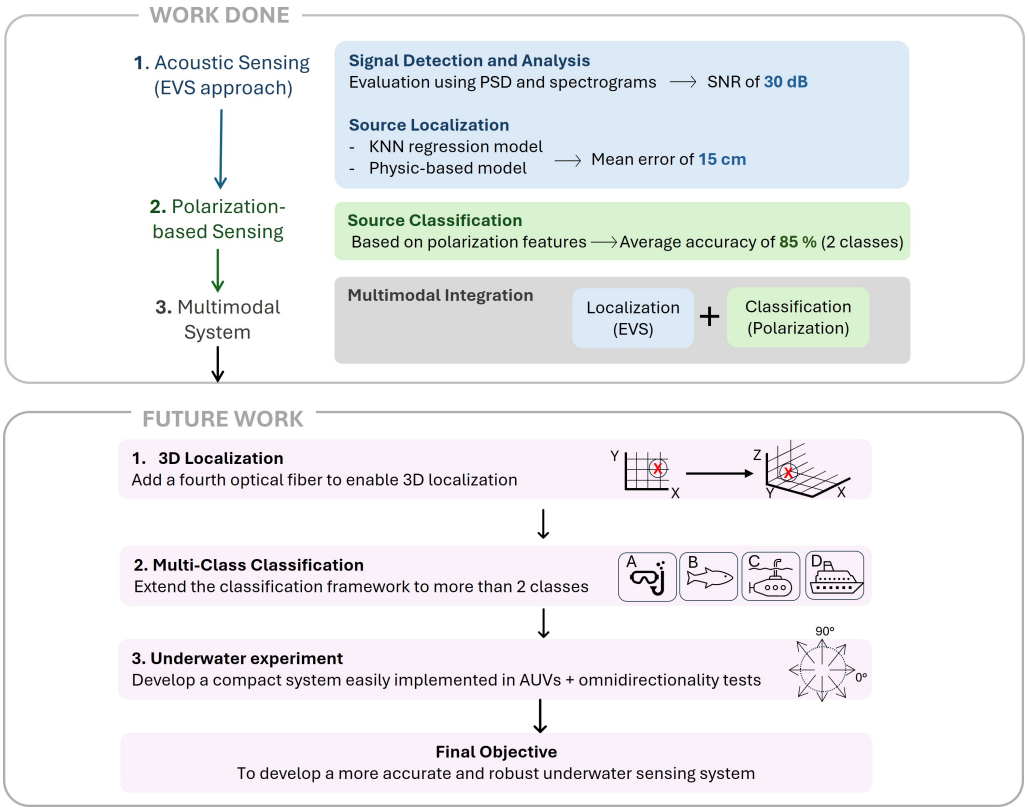

Figure 5.2: Overview of the sensing approaches investigated in this work and the main directions for future development.

References

[1] J. T. Xu, L. Luo, J. Saw, C. C. Wang, S. K. Sinha, R. Wolfe, K. Soga, Y. Wu, and M. DeJong, "Structural health monitoring of offshore wind turbines using distributed acoustic sensing (das)," *Journal of Civil Structural Health Monitoring*, vol. 15, pp. 445–463, 2 2025. [Cited on page 1.]

[2] D. Hill and P. Nash, "Fiber-optic hydrophone array for acoustic surveillance in the littoral," in *Proc.SPIE*, vol. 5780, 5 2005, pp. 1–10. [Online]. Available: https://doi.org/10.1117/12.607550 [Cited on page 1.]

[3] Y. Zhao, B. Yin, G. Sang, Z. Jiang, H. Li, B. Wu, L. Pei, and S. Wu, "Applications of optical fiber sensors in marine observation: a review," *Intelligent Marine Technology and Systems*, vol. 3, p. 38, 2025. [Online]. Available: https://doi.org/10.1007/s44295-025-00089-w [Cited on page 1.]

[4] B. A. Taha, A. J. Addie, A. J. Haider, S. A. Osman, M. Z. Ramli, and N. Arsad, "A review of seismic detection using fiber optic distributed acoustic sensing: from telecommunication cables to earthquake sensors," *Natural Hazards*, vol. 121, pp. 13 927–13 959, 2025. [Online]. Available: https://doi.org/10.1007/s11069-025-07370-5 [Cited on page 1.]

[5] Migatron Corporation. (2025) Ultrasonic sensors for oil & gas applications. Accessed: 2025-06-02. [Online]. Available: https://www.migatron.com/industries/oil-and-gas-sensors/ [Cited on pages vii and 1.]

[6] Y. Guo, J. M. Marin, I. Ashry *et al.*, "Submarine optical fiber communication provides an unrealized deep-sea observation network," *Scientific Reports*, vol. 13, p. 15412, 2023. [Cited on pages vii and 1.]

[7] H. Yang, Z. Xu, and B. Jia, "An underwater positioning system for uuvs based on lidar camera and inertial measurement unit," *Sensors*, vol. 22, 7 2022. [Cited on page 2.]

[8] K. Hu, T. Wang, C. Shen, C. Weng, F. Zhou, M. Xia, and L. Weng, "Overview of underwater 3d reconstruction technology based on optical images," *Journal of Marine Science and Engineering*, vol. 11, 5 2023. [Cited on page 3.]

[9] J. Zhang, G. Zhang, Y. Geng, Z. Bai, F. Zhang, H. Zhao, J. Chen, J. Hao, R. Wang, L. Jia, and W. Zhang, “A novel integrated scalar-vector hydrophone for enhanced low-frequency acoustic detection in marine environments,” *Measurement: Journal of the International Measurement Confederation*, vol. 256, 12 2025. [Cited on page 3.]

[10] L. Bouffaut, K. Taweesintananon, H. J. Kriesell, R. A. Rørstadbotnen, J. R. Potter, M. Landrø, S. E. Johansen, J. K. Brenne, A. Haukanes, O. Schjelderup, and F. Storvik, “Eavesdropping at the speed of light: Distributed acoustic sensing of baleen whales in the arctic,” *Frontiers in Marine Science*, vol. 9, 7 2022. [Cited on page 3.]

[11] U. Senkans, N. Silkans, S. Spolitis, and J. Braunfelds, “Recent advances in distributed optical sensing technologies based on rayleigh, brillouin and raman scattering,” in *2025 Photonics Electromagnetics Research Symposium - Fall (PIERS-Fall)*, 2025, pp. 1–9. [Cited on page 3.]

[12] *Dashed Against the Rocks - Comparison of Distributed Acoustic Sensing (DAS) Data and Physical Response Models of Subsea Cables*, ser. International Conference on Offshore Mechanics and Arctic Engineering, vol. Volume 5: Ocean Renewable Energy, 06 2025. [Online]. Available: https://doi.org/10.1115/OMAE2025-157573 [Cited on page 3.]

[13] Y. Wang, B. Xu, G. Chen, Z. Li, B. Du, X. Xu, Y. Wang, and J. He, “Suppression of doppler-induced crosstalk in linear-frequency-swept Φ-otdr using scattering-enhanced fiber,” *Optics Express*, vol. 33, p. 42358, 10 2025. [Cited on page 3.]

[14] EarthScope Consortium. (2025) Distributed acoustic sensing. EarthScope Consortium. [Online]. Available: https://www.earthscope.org/what-is/das/ [Cited on pages vii and 4.]

[15] S. Liang, C. Zhang, W. Lin, L. Li, C. Li, X. Feng, and B. Lin, “Fiber-optic intrinsic distributed acoustic emission sensor for large structure health monitoring,” *Opt. Lett.*, vol. 34, no. 12, pp. 1858–1860, Jun 2009. [Online]. Available: https://opg.optica.org/ol/abstract.cfm?URI=ol-34-12-1858 [Cited on page 4.]

[16] P. Fan, W. Yan, P. Lu, W. Zhang, W. Zhang, X. Fu, and J. Zhang, “High sensitivity fiber-optic michelson interferometric low-frequency acoustic sensor based on a gold diaphragm,” *Optics Express*, vol. 28, p. 25238, 8 2020. [Cited on page 4.]

[17] G. Zhang, C. Xi, Y. Liang, and H. Zuo, “Dual-sagnac optical fiber sensor used in acoustic emission source location,” in *Proceedings of 2011 Cross Strait Quad-Regional Radio Science and Wireless Technology Conference*, vol. 2, 2011, pp. 1598–1602. [Cited on page 4.]

[18] J. Ma, Y. Yu, and W. Jin, “Demodulation of diaphragm based acoustic sensor using sagnac interferometer with stable phase bias,” *Opt. Express*, vol. 23, no. 22, pp. 29 268–29 278, Nov 2015. [Online]. Available: https://opg.optica.org/oe/abstract.cfm?URI=oe-23-22-29268 [Cited on page 4.]

[19] P. Wang, Y. Pan, J. Zhang, J. Zhai, D. Liu, and P. Lu, “Miniaturized and highly sensitive fiber-optic fabry-perot sensor for mhz infrasound detection,” *Photon. Res.*, vol. 12, no. 5, pp. 969–978, May 2024. [Online]. Available: https://opg.optica.org/prj/abstract.cfm?URI=prj-12-5-969 [Cited on page 4.]

[20] A. Wang, X. Fan, G. Chen, Y. Liu, Z. Li, Z. Zhang, X. Wang, F. Zhang, Z. Zhang, H. Qiu, H. Gao, W. Xiong, H. Li, and Q. Sun, “Ultrahigh-sensitivity 3d-printed hollow fabry-pérot fiber ultrasound sensor for photoacoustic imaging,” *ACS Photonics*, vol. 12, no. 8, pp. 4553–4562, 07 2025. [Online]. Available: https://doi.org/10.1021/acsphotonics.5c00944 [Cited on page 4.]

[21] J. Johny, T. Smith, K. Bhavsar, and R. Prabhu, “Design of optical fibre based highly sensitive acoustic sensor for underwater applications,” in *OCEANS 2017 - Aberdeen*, 2017, pp. 1–5. [Cited on page 4.]

[22] J. Wang, F. Ai, Q. Sun, T. Liu, H. Li, Z. Yan, and D. Liu, “Diaphragm-based optical fiber sensor array for multipoint acoustic detection,” *Optics Express*, vol. 26, p. 25293, 9 2018. [Cited on page 4.]

[23] B. Nan, W. Bao, Z. Shao, C. Liao, X. Sun, and Y. Wang, “A 3d-printed multicore fiber-tip resonator for ultrasonic sensing,” *ACS Photonics*, vol. 12, pp. 6114–6121, 11 2025. [Cited on page 4.]

[24] J. Pan, Q. Li, Y. Feng, R. Zhong, Z. Fu, S. Yang, W. Sun, B. Zhang, Q. Sui, J. Chen, Y. Shen, and Z. Li, “Parallel interrogation of the chalcogenide-based micro-ring sensor array for photoacoustic tomography,” *Nature Communications*, vol. 14, 12 2023. [Cited on page 4.]

[25] Q. Rong, Y. Lee, Y. Tang, T. Vu, C. Taboada, W. Zheng, J. Xia, D. A. Czaplewski, H. F. Zhang, C. Sun, and J. Yao, “High-frequency 3d photoacoustic

computed tomography using an optical microring resonator," *BME Frontiers*, vol. 2022, 2022. [Online]. Available: https://www.sciencedirect.com/science/article/pii/S2765803122000128 [Cited on page 4.]

[26] R. Chen, G. F. Fernando, T. Butler, and R. A. Badcock, "A novel ultrasound fibre optic sensor based on a fused-tapered optical fibre coupler," *Measurement Science and Technology*, vol. 15, no. 8, p. 1490, jul 2004. [Online]. Available: https://doi.org/10.1088/0957-0233/15/8/010 [Cited on page 4.]

[27] N. K. Mohan, "Speckle methods and applications," in *Handbook of Optical Metrology*, 2nd ed. CRC Press, 2015, p. 23. [Cited on page 5.]

[28] J. Goodman, *Speckle Phenomena in Optics: Theory and Applications*. Roberts & Company, 2007. [Online]. Available: https://books.google.pt/books?id=TynXEcS0DncC [Cited on page 5.]

[29] A. Wang, J. Wang, Z. Gan, G. Yue, X. Chen, Q. Yan, S. Wang, Y. Yan, T. Geng, S. Chen, and W. Sun, "Influence of optical fiber parameters on the speckle pattern and spectral observation in astronomy," *Photonics*, vol. 11, no. 11, 2024. [Online]. Available: https://www.mdpi.com/2304-6732/11/11/1056 [Cited on page 5.]

[30] I. Chapalo, A. Stylianou, P. Mégret, and A. Theodosiou, "Advances in optical fiber speckle sensing: A comprehensive review," *Photonics*, vol. 11, no. 4, p. 299, 2024. [Cited on pages 5 and 7.]

[31] A. G. Leal-Junior, A. Frizera, C. Marques, and M. J. Pontes, "Optical fiber specklegram sensors for mechanical measurements: A review," *IEEE Sensors Journal*, vol. 20, no. 2, pp. 569–576, 2020. [Cited on page 5.]

[32] D. Pal, S. Agadarov, Y. Beiderman *et al.*, "Non-invasive blood glucose sensing by machine learning of optic fiber-based speckle pattern variation," *Journal of Biomedical Optics*, vol. 27, no. 9, p. 097001, Sep. 2022. [Cited on page 5.]

[33] O. Galicio, J. Calvo, T. Leyva, M. Saavedra, S. Lopez, A. Baldárrago, and O. Chamorro, "Electronic system to speckle phenomenon characterization for random movement on fiber optics," *Indonesian Journal of Electrical Engineering and Computer Science*, vol. 36, p. 1409, 12 2024. [Cited on pages 6 and 37.]

[34] R. Paschotta, “Higher-order modes,” RP Photonics Encyclopedia, available online at https://www.rp-photonics.com/higher_order_modes.html. [Online]. Available: https://www.rp-photonics.com/higher_order_modes.html [Cited on page 6.]

[35] ——, “Mode coupling,” RP Photonics Encyclopedia, available online at https://www.rp-photonics.com/mode_coupling.html. [Online]. Available: https://www.rp-photonics.com/mode_coupling.html [Cited on page 7.]

[36] T. Lopes, J. M. Teixeira, T. D. Ferreira, C. S. Monteiro, P. A. S. Jorge, and N. A. Silva, “All-optical edge computing for speckle sensing interrogation,” 2026. [Online]. Available: https://arxiv.org/abs/2605.25805 [Cited on page 7.]

[37] L. Costa, S. Varughese, P. Mertz, V. Kamalov, and Z. Zhan, “Localization of seismic waves with submarine fiber optics using polarization-only measurements,” *Communications Engineering*, vol. 2, 12 2023. [Cited on pages 8 and 37.]

[38] J. R. Serres, P.-J. Lapray, S. Viollet, T. Kronland-Martinet, A. Moutenet, O. Morel, and L. Bigué, “Passive polarized vision for autonomous vehicles: A review,” *Sensors*, vol. 24, no. 11, 2024. [Online]. Available: https://www.mdpi.com/1424-8220/24/11/3312 [Cited on page 8.]

[39] C. Taglione, C. Mateo, and C. Stolz, “Polarimetric imaging for robot perception: A review,” *Sensors*, vol. 24, no. 14, 2024. [Online]. Available: https://www.mdpi.com/1424-8220/24/14/4440 [Cited on page 8.]

[40] S. B. Karman, S. Z. M. Diah, and I. C. Gebeshuber, “Bio-inspired polarized skylight-based navigation sensors: A review,” *Sensors*, vol. 12, no. 11, pp. 14 232–14 261, 2012. [Online]. Available: https://www.mdpi.com/1424-8220/12/11/14232 [Cited on page 8.]

[41] G. Cohen, S. Afshar, B. Morreale, T. Bessell, A. Wabnitz, M. Rutten, and A. van Schaik, “Event-based sensing for space situational awareness,” *Journal of the Astronautical Sciences*, vol. 66, pp. 125–141, 6 2019. [Cited on page 8.]

[42] FRAMOS Technologies, “Event-based vision sensors,” https://www.framos.com/en/products-solutions/image-sensors/technologies/event-based-sensors, 2023, accessed: 2026-06-01. [Cited on page 8.]

[43] Sony Semiconductor Solutions, “Event-based vision sensor (evs) technology,” https://www.sony-semicon.com/en/technology/industry/evs.html, 2023, accessed: 2026-06-01. [Cited on page 8.]

[44] T. Lopes, J. Teixeira, V. V. Rocha, T. D. Ferreira, C. S. Monteiro, P. A. S. Jorge, and N. A. Silva, “Event-based speckle interrogation for high-bandwidth multi-point optical fiber sensing,” Tech. Rep. [Cited on page 10.]

[45] A. Tokovinin, “Performance of the soar speckle instrument,” *The Astronomical Journal*, vol. 168, no. 3, p. 125, aug 2024. [Online]. Available: https://doi.org/10.3847/1538-3881/ad6153 [Cited on page 10.]

[46] F. Arı, H. Şerbetçi, and İsa Navruz, “Tapered fiber optic refractive index sensor using speckle pattern imaging,” *Optical Fiber Technology*, vol. 79, p. 103366, 2023. [Online]. Available: https://www.sciencedirect.com/science/article/pii/S1068520023001463 [Cited on page 10.]

[47] O. A. O. Galicio, J. L. Calvo, T. N. D. Leyva, M. M. Saavedra, S. A. S. Lopez, A. C. Baldárrago, and O. C. Atalaya, “Electronic system to speckle phenomenon characterization for random movement on fiber optics,” *Indonesian Journal of Electrical Engineering and Computer Science*, vol. 36, no. 3, pp. 1409–1420, 2024. [Cited on page 10.]

[48] Astrobasics. (2022) Ccd or cmos. Accessed: 2025-06-02. [Online]. Available: https://astrobasics.de/en/components/camera/ccd-or-cmos/ [Cited on pages vii and 12.]

[49] B. Chakravarthi, A. A. Verma, K. Daniilidis, C. Fermuller, and Y. Yang, “Recent event camera innovations: A survey,” in *Computer Vision – ECCV 2024 Workshops*, A. Del Bue, C. Canton, J. Pont-Tuset, and T. Tommasi, Eds. Cham: Springer Nature Switzerland, 2025, pp. 342–376. [Cited on page 12.]

[50] Teledyne Vision Solutions. (n.d.) Ccd vs cmos. [Online]. Available: https://www.teledynevisionsolutions.com/en-150/learn/learning-center/imaging-fundamentals/ccd-vs-cmos/ [Cited on pages vii and 13.]

[51] Canon. (n.d.) Cmos sensors. [Online]. Available: https://canon-cmos-sensors.com/cmos-sensors/ [Cited on pages vii and 13.]

[52] G. Guo, Y. Feng, H. Lv, Y. Zhao, H. Liu, and G. Bi, “Event-guided image super-resolution reconstruction,” *Sensors*, vol. 23, 2 2023. [Cited on pages vii and 14.]

[53] M. Gehrig and D. Scaramuzza, “Recurrent vision transformers for object detection with event cameras,” in *Proceedings of the IEEE/CVF Conference on Computer Vision and Pattern Recognition (CVPR)*, 2023, pp. 13 884–13 893. [Cited on page 15.]

[54] J. Manderscheid, A. Sironi, N. Bourdis, D. Migliore, and V. Lepetit, “Speed invariant time surface for learning to detect corner points with event-based cameras,” in *2019 IEEE/CVF Conference on Computer Vision and Pattern Recognition (CVPR)*, 2019, pp. 10 237–10 246. [Cited on page 15.]

[55] A. Sironi, M. Brambilla, N. Bourdis, X. Lagorce, and R. Benosman, “Hats: Histograms of averaged time surfaces for robust event-based object classification,” in *Proceedings of the IEEE Conference on Computer Vision and Pattern Recognition (CVPR)*, 2018, pp. 1731–1740. [Cited on page 15.]

[56] A. Censi and D. Scaramuzza, “Low-latency event-based visual odometry,” in *2014 IEEE International Conference on Robotics and Automation (ICRA)*. IEEE, 2014, pp. 703–710. [Cited on page 15.]

[57] M. Shahraki, A. Elamin, and A. El-Rabbany, “Event-based visual simultaneous localization and mapping (evslam) techniques: State of the art and future directions,” *Journal of Sensor and Actuator Networks*, vol. 14, no. 1, 2025. [Online]. Available: https://www.mdpi.com/2224-2708/14/1/7 [Cited on page 15.]

[58] R. Benosman, S. H. Ieng, C. Clercq, C. Bartolozzi, and M. Srinivasan, “Asynchronous frameless event-based optical flow,” *Neural Networks*, vol. 27, pp. 32–37, 3 2012. [Cited on page 15.]

[59] Y. Nam, M. Mostafavi, K.-J. Yoon, and J. Choi, “Stereo depth from events cameras: Concentrate and focus on the future,” in *2022 IEEE/CVF Conference on Computer Vision and Pattern Recognition (CVPR)*, 2022, pp. 6104–6113. [Cited on page 15.]

[60] P. Zhang, H. Liu, Z. Ge, C. Wang, and E. Y. Lam, “Neuromorphic imaging with joint image deblurring and event denoising,” *IEEE Transactions on Image Processing*, vol. 33, pp. 2318–2333, 2024. [Cited on page 15.]

[61] Prophesee. (2025) Event-based sensor imx636 sony prophesee. [Online]. Available: https://www.prophesee.ai/event-based-sensor-imx636-sony-prophesee/ [Cited on page 15.]

[62] Y. Koike and M. Asai, “The future of plastic optical fiber,” *NPG Asia Materials*, vol. 1, no. 1, pp. 22–28, 2009. [Cited on page 20.]

[63] F. Uyar, A. S. Aldemir, T. Kartaloglu, E. Ozbay, and I. Ozdur, “A compliant mandrel-based fiber-optic hydrophone for underwater acoustic sensing,” *IEEE Sensors Journal*, vol. 25, pp. 34 671–34 680, 2025. [Cited on page 22.]

[64] M. Fajkus, J. Nedoma, R. Martinek, M. Fridrich, E. Bednar, S. Zabka, and P. Zmij, “Pressure membrane fbg sensor realized by 3d technology,” *Sensors*, vol. 21, no. 15, 2021. [Online]. Available: https://www.mdpi.com/1424-8220/21/15/5158 [Cited on page 22.]

[65] L. Maya, L. Fan, A. Durocher, C. Willert *et al.*, “An evaluation of event-based cameras for particle image velocimetry,” *Experiments in Fluids*, vol. 66, p. 204, 2025. [Online]. Available: https://doi.org/10.1007/s00348-025-04127-5 [Cited on page 24.]

[66] G. G. Stokes, “On the Composition and Resolution of Streams of Polarized Light from different Sources,” *Transactions of the Cambridge Philosophical Society*, vol. 9, p. 399, 1851. [Cited on page 34.]

[67] H. Poincaré, *Théorie mathématique de la lumière II.: Nouvelles études sur la diffraction.–Théorie de la dispersion de Helmholtz*. Georges Carré, 1892. [Cited on page 35.]

[68] Z. Yu, J. Yang, C. Lin, X. Zhang, F. Dang, Y. Yuan, L. Yuan, Y. Wang, and Y. Qin, “Distributed polarization measurement for fiber sensing coils: A review,” *Journal of Lightwave Technology*, vol. 39, no. 12, pp. 3699–3710, 2021. [Cited on page 37.]

[69] A. Mecozzi, M. Cantono, J. C. Castellanos, V. Kamalov, R. Muller, and Z. Zhan, “Polarization sensing using submarine optical cables,” *Optica*, vol. 8, no. 6, pp. 788–795, Jun 2021. [Online]. Available: https://opg.optica.org/optica/abstract.cfm?URI=optica-8-6-788 [Cited on page 37.]

[70] Z. Zhan, M. Cantono, V. Kamalov, A. Mecozzi, R. Müller, S. Yin, and J. C. Castellanos, “Optical polarization–based seismic and water wave sensing on transoceanic cables,” *Science*, vol. 371, no. 6532, pp. 931–936, 2021. [Online]. Available: https://www.science.org/doi/abs/10.1126/science.abe6648 [Cited on page 37.]

[71] C. Caucheteur, T. Guo, and J. Albert, “Polarization-assisted fiber bragg grating sensors: Tutorial and review,” *Journal of Lightwave Technology*, vol. 35, no. 16, pp. 3311–3322, 2017. [Cited on page 37.]

[72] Y. Kim, T. Noh, Y. Lee, E.-S. Kim, B. Shin, and S.-M. Lee, “Fiber-optic hydrogen sensor based on polarization-diversity loop interferometer,” *Journal of the Korean Physical Society*, vol. 62, 02 2013. [Cited on page 37.]

[73] M. Yang, Z. Sha, and F. Zhang, “A multimodal approach based on large vision model for close-range underwater target localization,” *IEEE/ASME Transactions on Mechatronics*, vol. 30, no. 4, pp. 2427–2437, 2025. [Cited on page 45.]

[74] ——, “Learning-based leader localization for underwater vehicles with optical-acoustic-pressure sensor fusion,” *IEEE/ASME Transactions on Mechatronics*, vol. 31, no. 2, pp. 1334–1345, 2026. [Cited on page 45.]

[75] Active Silicon. (n.d.) Rov camera and vision technology. [Online]. Available: https://www.activesilicon.com/capabilities/rov-camera-and-vision-technology/ [Cited on pages viii and 51.]